

## INFORMATION TO USERS

This manuscript has been reproduced from the microfilm master. UMI films the text directly from the original or copy submitted. Thus, some thesis and dissertation copies are in typewriter face, while others may be from any type of computer printer.

**The quality of this reproduction is dependent upon the quality of the copy submitted.** Broken or indistinct print, colored or poor quality illustrations and photographs, print bleedthrough, substandard margins, and improper alignment can adversely affect reproduction.

In the unlikely event that the author did not send UMI a complete manuscript and there are missing pages, these will be noted. Also, if unauthorized copyright material had to be removed, a note will indicate the deletion.

Oversize materials (e.g., maps, drawings, charts) are reproduced by sectioning the original, beginning at the upper left-hand corner and continuing from left to right in equal sections with small overlaps. Each original is also photographed in one exposure and is included in reduced form at the back of the book.

Photographs included in the original manuscript have been reproduced xerographically in this copy. Higher quality 6" x 9" black and white photographic prints are available for any photographs or illustrations appearing in this copy for an additional charge. Contact UMI directly to order.

# UMI

A Bell & Howell Information Company  
300 North Zeeb Road, Ann Arbor MI 48106-1346 USA  
313/761-4700 800/521-0600



*The LORD is my rock, my fortress and my deliverer; my God is my rock, in whom I take refuge. He is my shield and the horn of my salvation, my stronghold.*

Psalm 18:2



UNIVERSITY OF ALBERTA

**Comparative Studies on Microwave Fiber Optic Links  
used for Personal Communication Systems**

BY

**Bun Endymion Yeung**



A thesis submitted to the Faculty of Graduate Studies and Research in partial fulfilment of the requirements for the degree of **Master of Science**.

DEPARTMENT OF ELECTRICAL AND COMPUTER ENGINEERING

EDMONTON, ALBERTA

SPRING 1998



National Library  
of Canada

Bibliothèque nationale  
du Canada

Acquisitions and  
Bibliographic Services

Acquisitions et  
services bibliographiques

395 Wellington Street  
Ottawa ON K1A 0N4  
Canada

395, rue Wellington  
Ottawa ON K1A 0N4  
Canada

*Your file* *Votre référence*

*Our file* *Notre référence*

The author has granted a non-exclusive licence allowing the National Library of Canada to reproduce, loan, distribute or sell copies of this thesis in microform, paper or electronic formats.

L'auteur a accordé une licence non exclusive permettant à la Bibliothèque nationale du Canada de reproduire, prêter, distribuer ou vendre des copies de cette thèse sous la forme de microfiche/film, de reproduction sur papier ou sur format électronique.

The author retains ownership of the copyright in this thesis. Neither the thesis nor substantial extracts from it may be printed or otherwise reproduced without the author's permission.

L'auteur conserve la propriété du droit d'auteur qui protège cette thèse. Ni la thèse ni des extraits substantiels de celle-ci ne doivent être imprimés ou autrement reproduits sans son autorisation.

0-612-29001-8

**Canada**

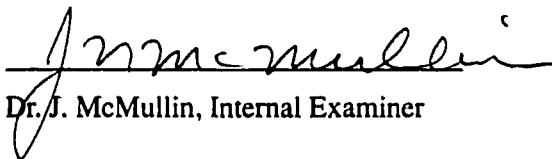
UNIVERSITY OF ALBERTA

Faculty of Graduate Studies and Research

The undersigned certify that they have read, and recommend to the Faculty of Graduate Studies and Research for acceptance, a thesis entitled **Comparative Studies on Microwave Fiber Optic Links used for Personal Communication Systems** submitted by **Bun Endymion Yeung** in partial fulfillment of the requirements for the degree of **Master of Science**.



Dr. R.I. MacDonald, Supervisor



Dr. J. McMullin, Internal Examiner



Dr. W. Allegretto, External Examiner

Date: 22/1/98

## ABSTRACT

Future personal communication systems require a large number of cells to cover the service area. In order to reduce the cost, all the expensive equipment such as control and logic equipment should be located at one central site and all the remote sites should have only inexpensive antenna units. This technique is called antenna remoting. Microwave fiber optic link is a good transmission medium to carry information between the central site and the remote antenna sites because of its low cost and low loss.

Several microwave fiber optic links that can be used for the microcellular communication systems, including direct modulation/ direct detection fiber optic link (DM/DD FOL), DM/DD FOL with frequency conversion at the antenna sites, externally modulation/ direct detection (EM/DD) FOL and fiber optic mixing links have been discussed.

The performance analysis in term of carrier-to-noise ratio (CNR) of a simple DD/DM system, a DD/DM system using an optoelectronic mixer (OEM), and a cascaded modulator loop system are presented. An economic discussion of latter two systems is also presented. The cascaded modulator loop system is more cost-effective than the DD/DM system using an OEM.



## ACKNOWLEDGEMENTS

I wish to express my sincere gratitude to my supervisor, Dr. R. Ian MacDonald for his support, encouragement and guidance throughout the course of my project work.

I would like to extend my sincere thanks to Dr. Q.Z. Liu for his help in the early stage of this project. I also thanks Mr. David Clegg for his help in the laboratory. I am thankful to Mr. David Boertjes, Mr. Sheldon Walklin, Mr. Craig Unick, Mr. Sing Cheng, and Mr. Songsong Sun for their stimulating discussions.

I thank Telecommunication Research Laboratories for the award of a TR Labs Graduate Research Scholarship in Photonics. TR Labs has been a center for the higher learning and applied research in advanced telecommunications and I am proud to be a member in the Photonics research team.

Lastly, I would like to express my love and sincere gratitude to my family and friends for their continued support and encouragement.

# Table of Contents

<b>1.0</b>	<b>INTRODUCTION</b>	<b>1</b>
1.1	Concept of Cellular Communication	1
1.2	Microcellular and Personal Communication Systems	1
1.3	Thesis Outline	2
<b>2.0</b>	<b>MICROWAVE FIBER OPTIC LINKS</b>	<b>3</b>
2.1	Direct Modulation / Direct Detection (DM/DD) fiber optic link	4
2.2	DM/DD fiber optic links with frequency up-conversion at the receiver site	6
2.2.1	using twin links	7
2.2.2	using sub-harmonic injection technique	7
2.2.3	using frequency or wavelength division multiplexing	10
2.2.4	using opto-electronic mixers (OEMs)	11
2.3	Externally Modulated fiber optic links	12
2.4	Fiber optic mixing links	13
2.4.1	Dual mixing link	13
2.4.2	Harmonic laser diode mixing link	14
2.5	Proposed systems for analysis	15
<b>3.0</b>	<b>THEORY</b>	<b>20</b>
3.1	Laser Diode	20
3.1.1	The concept of stimulated emission	20
3.1.2	Direct current modulation of semiconductor lasers	22
3.2	External Modulator	27
3.3	Photodetector	29
3.3.1	PIN photodiode	29
3.3.2	MMSM photodetector	31
3.4	Noise	33
3.4.1	Thermal noise	33
3.4.2	Shot noise	34
3.4.3	Relative intensity noise	34
3.4.4	Intermodulation noise	35
<b>4.0</b>	<b>PROPOSED SYSTEMS PERFORMANCE ANALYSIS</b>	<b>37</b>
4.1	DM/DD	37
4.2	DM/DD using an OEM	43
4.3	External modulators loop	47
4.3.1	Up-link system	47
4.3.2	Down-link system	51
<b>5.0</b>	<b>EXPERIMENT RESULTS</b>	<b>55</b>
5.1	Modulators characteristics	55
5.1.1	CRC lightwave testset	55
5.1.2	EOTEK 2X2 electro-optic switch	56
5.2	Harmonics generation of the Mach Zehnder modulator	58
5.3	Two cascaded stages test	61
5.4	Single stage test	71
5.5	Mixing properties	75
5.6	Summary	79

6.0	ECONOMIC ANALYSIS ON THE PROPOSED LINKS	81
6.1	Physical layout	81
6.2	Number of components	83
7.0	CONCLUSION	85
7.1	Thesis review	85
7.2	Future works	87
8.0	REFERENCES	88
9.0	APPENDIX	92

## *List of Tables*

TABLE 1.	Parameters used for calculating the transfer characteristics of laser diodes	
	26	
TABLE 2.	Coefficients at different temperature	27
TABLE 3.	Parameters used to calculate CNR	41
TABLE 4.	Parameters in calculating CNR of the OEM loop system	50

## *List of Figures*

FIG. 1 Direct modulation/ Direct detection link	4
FIG. 2 Magnitude of material and waveguide dispersion as a function of optical wavelength for a single-mode fused-silica-core fiber.[16]	6
FIG. 3 DM/DD using twin link	7
FIG. 4 Schematic illustration of direct optical injection-locking technique of a CW IMPATT oscillator	8
FIG. 5 Schematic illustration of indirect optical injection-locking	9
FIG. 6 Frequency up-conversion using frequency multiplexing	10
FIG. 7 Fiber optic link using WDM	11
FIG. 8 Microwave fiber optic link using OEM	11
FIG. 9 External modulation link	13
FIG. 10 Dual mixing link	13
FIG. 11 Harmonic laser mixing link	14
FIG. 12 DM/DD system using OEM	16
FIG. 13 Link configuration with cascaded radio base stations	17
FIG. 14 Detailed configuration of the up-link system of the loop configuration	17
FIG. 15 Detailed configuration of the down-link system of the loop configuration	19
FIG. 16 The three vital transition processes in laser action.	21
FIG. 17 Output light versus input diode current	22
FIG. 18 Output Light versus Diode Current	26
FIG. 19 Structure of a Mach-Zehnder modulator	28
FIG. 20 Transfer characteristics of an EOM	29
FIG. 21 Schematic representation of a reverse-biased one-dimensional PIN photodiode	30
FIG. 22 DC responsivity of the MSM PD	32
FIG. 23 Relationship of signals and IMD	36
FIG. 24 CNR performance of the DM/DD link at 0 oC	41
FIG. 25 CNR performance of the DM/DD link at 40 oC	42
FIG. 26 CNR performance of the DM/DD link with temperature as a parameter	42

FIG. 27	CNR performance of the DM/DD link with channel BW as a parameter	43
FIG. 28	CNR of the DM/DD link using OEM at 0 oC	45
FIG. 29	CNR of the DM/DD link using OEM at 40 oC	45
FIG. 30	CNR of the DM/DD link using OEM with temperature as a parameter	46
FIG. 31	CNR of the DM/DD link using OEM with channel as a parameter	46
FIG. 32	CNR performance of the up-link system	51
FIG. 33	CNR performance of the down-link system	54
FIG. 34	CNR of the down-link system with mLO as a parameter	54
FIG 35.	Transfer characteristic of the CRC testset	56
FIG 36.	Physical structure of a balanced bridge interferometer	57
FIG 37.	Transfer characteristic of the ETEK 2X2 electro-optic switch	58
FIG 38.	Experimental setup for harmonic measurement	59
FIG 39.	Signal power versus DC bias voltage of the Mach-Zehnder modulator: a) fundamental, b) first harmonic, c) second harmonic, d) third harmonic.	60
FIG 40.	Experimental setup for the two stages test	61
FIG 41.	Frequency spectrum for the two stages test	63
FIG 42.	CIR as a function of modulation index (two stages test). (a) channel 1, (b) channel 2	64
FIG 43.	Power of the channel two signal and the intermodulation product at 1.6 GHz as a function of the DC bias voltage of modulator one.	66
FIG 44.	CIR of channel two as a function of DC bias voltage of modulator one.	67
FIG 45.	Power of the channel one signal and the intermodulation product at 700 MHz as a function of the DC bias voltage of modulation two.	68
FIG 46.	CIR of channel one as a function of DC bias voltage of modulator two.	69
FIG 47.	SPDR for channel one	70
FIG 48.	SPDR for channel two	70
FIG 49.	Experimental setup for single stage test	71
FIG 50.	Frequency spectrum of the single stage test	72
FIG 51.	CIR of channel one versus RF input power (single stage test)	73
FIG 52.	CIR of channel two versus RF input power (single stage test)	73
FIG 53.	SPDR of channel one. (single stage test)	74
FIG 54.	SPDR of channel two. (single stage test)	74
FIG 55.	Experimental setup for frequency conversion measurement	76
FIG 56.	Frequency spectrum of the frequency conversion test.	76

FIG 57. Power of frequency down-converted signal as a function of DC bias voltage of the modulator. (RF input 0 dBm and 15 dBm)	77
FIG 58. Power of frequency up-converted signal as a function of DC bias voltage of the modulator. (RF input 0 dBm and 15 dBm)	78
FIG 59. Power of frequency down-converted signal as a function of DC bias voltage of the modulator. (RF input -15 dBm and 10 dBm)	78
FIG 60. Power of frequency up-converted signal as a function of DC bias voltage of the modulator. (RF input -15 dBm and 10 dBm)	79
FIG 61. Physical layout of the cascaded modulators loop system.	81
FIG 62. Physical layout of the direct link system.	82

# **1.0 INTRODUCTION**

## **1.1 Concept of Cellular Communication**

During the late 1960s, the Bell System proposed a new method to solve the problem of spectrum congestion by reconstructing the coverage areas of mobile radio systems. The traditional approach was to set up a high power transmitter at the highest point in the coverage area. The mobile units needed to have a line of sight to the transmitter for adequate radio coverage. Line of sight transmission is limited to the distance to the horizon (approximately 70 to 80 km from the transmitter). Therefore, the system provided a limited coverage area and it allowed only a limited number of users.

The cellular communication system handles the coverage problem differently. It does not use the broadcasting method; rather it uses a large number of low-power transmitters designed to cover a small area. Therefore, instead of covering the whole city by a single transmitter, the city is divided into many smaller coverage areas called 'cells'. By reducing the total coverage area into small cells, it becomes possible to reuse the same frequency in different cells. The problem of using small cells is that a call may not be finished within a single cell. To solve this problem, the idea of handoff is introduced. Handoff occurs when a mobile is about to cross a cell border. When the user is approaching the border, the received signal power at the original site is decreasing. At the same time, one of the surrounding sites with the strongest received signal will become the next host site. When the user enters the new site, the old site will pass all the control information to the new site and the handoff is completed.

## **1.2 Microcellular and Personal Communication Systems**

Due to the rapid increase in the number of mobile telephone users, cell splitting and other technologies such as CDMA (code-division multiple access) are used to increase



the system's capacity. Continuously decreasing the cell size due to cell splitting has led to the introduction of microcellular and personal communication systems. A microcellular system is referred to as a system with the cell size less than 300m. If the cell size is further reduced to about 20m, it is called the pico-cellular system. Since the cell size is decreased, a larger number of cells is required to cover the service area. It is very expensive to have a set of control equipment installed in every cell. This leads to the idea of antenna remoting. With remote antenna sites, all the expensive equipment will be located at a central processing site, while at the antenna sites, only a transmitter and receiver are installed. This can greatly reduce the overall system cost since the antenna sites, though numerous, are very compact and inexpensive. The small antenna unit also removes any necessity to acquire real estate. There is, however, a need to carry signals ready for broadcast to the transmitter and unprocessed signals back from the receiver. Fiber optic links seem to be a good method for carrying the information between the central site and the remote antenna sites because of their low loss, small size and light weight.

### **1.3 Thesis Outline**

In chapter 2, a number of microwave fiber optic links are introduced. The theory for different components of a fiber optic link is covered in chapter 3. The carrier-to-noise ratio (CNR) analyses of three proposed systems are covered in chapter 4. In chapter 5, the experimental results are presented. An economical comparison of two different system layouts is discussed. Finally, a conclusion is given in chapter 7.

## 2.0 MICROWAVE FIBER OPTIC LINKS

The integration of advanced mobile radio technologies into future networks involving microwave fiber optic technology has recently been intensively studied [1][2][3]. In the last decade, subcarrier multiplexed transmission over optical fiber has been developed for multichannel video distribution. Since the introduction of micro-cellular and pico-cellular personal communication systems, the microwave fiber optic link has been considered to be a good transport system for carrying information between a central office and the remote antenna sites because of its low loss, light weight and large capacity [4]. Microwave and millimetre-wave subcarrier transmission over the fiber optic links has been attempted using different methods including direct modulation of semiconductor lasers, external modulation, and heterodyne techniques based on semiconductor laser diode and photodiode nonlinearities [5][6][7]. The highest speed of direct modulation of a commercial semiconductor laser is about 30 GHz [8] which would be adequate for most foreseeable PCS systems. However, high speed semiconductor lasers usually require very sophisticated equipment for their manufacture and the prices for these devices are usually very high. On the other hand, optical modulators (EOMs), such as Mach-Zehnder interferometers, can be used to modulate light from a simple laser at the millimetre-wave band easily [9]. However, EOMs require high driving voltage and there are additional optical insertion losses. At the receiver side, relatively inexpensive PIN photodiodes are capable of directly detecting signals at about 60 GHz which is sufficient for the PCS, and there appears to be no real technology limitation.

To avoid transmitting high frequency optical signal, frequency conversion can be performed at the remote antenna site to shift the signals up to the radio frequency (RF). Many devices, such as MESFETs, HEMTs, and HBTs have been demonstrated as optoelectronic mixers (OEMs) [10][11]. Recently, at TRILabs, a system employing a MSM

photodiode as an OEM has been demonstrated [12][13]. The MSM-PD can be used as an integrated transceiver that can simplify the complexity and the cost of the receiver.

Some fiber optic millimetre-wave SCM transmission systems are reviewed in the following subsections.

## 2.1 Direct Modulation / Direct Detection (DM/DD) fiber optic link

The DM/DD fiber optic link is the simplest configuration but it requires more advanced equipment for transmitting signals at the millimetre-wave band. For the PCS operating in the millimetre-wave band, since the cell size is very small, a large number of cells is necessary to cover the service area. Therefore, it may not be cost-effective at present to employ DM/DD links for the PCS. The link configuration is shown in FIG. 1.

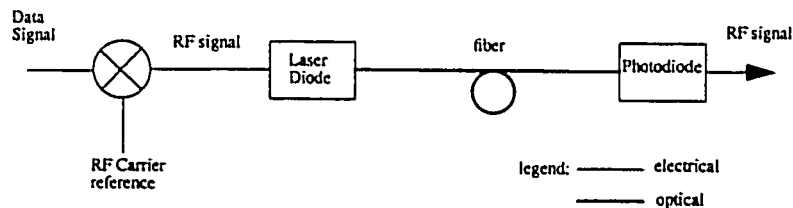


*FIG. 1 Direct modulation / Direct detection link*

This link consists of a semiconductor laser, a photodiode, and an optical fiber acting as the transmission medium. The baseband signal or the information signal is mixed with a single frequency signal at the local oscillator frequency at a conventional microwave mixer. The upconverted RF signal then drives the laser diode and the intensity of the output light of the laser diode is modulated according to the signal. The optical signal is then transmitted to the receiver site via the optical fiber. The signal is then detected

and converted to the electrical signal by a photodetector (a PIN photodiode typically). Finally, the signal can be electrically amplified and radiated at the antenna.

The main advantage of this link is the small number of components required and the potentially large link gain. Because of these, the size of the antenna packages can be very small. However the highest frequency that can be transmitted in this link is limited by the bandwidth of the laser diode. Commercial packages of semiconductor lasers that are capable of being directly intensity modulated at tens of GHz (millimetre-wave band) are still very expensive. The dispersion of the optical fiber causes an additional problem.

The dispersion in a single mode fiber is caused by both material and waveguide dispersions. The variation of the refractive index of the core material with wavelength is material dispersion. Material dispersion causes the light in the fiber to travel at different speeds for different wavelengths [14]. As a result, a narrow pulse, which has a wide spectrum, after propagating through the fiber will be either broadened or shrunk at the output depending on the sign of the dispersion at the particular wavelength. The variation in the modal propagation constant  $\beta$  with the ratio  $a/\lambda$ , where  $a$  is the core radius and  $\lambda$  is the wavelength of the propagating light, constitutes the waveguide dispersion. Waveguide dispersion causes the speed of signals in the fiber to attain an effective value which is between the velocities in the core, and the cladding material. As the refractive index is a function of wavelength, this type of dispersion causes pulse broadening. The sum of these two dispersions is the total dispersion for a single mode fiber. In FIG. 2, the material dispersion, the waveguide dispersion and the total dispersion of a typical single mode, fused-silica-core fiber are shown.

A millimetre-wave signal at 20 GHz carried by a 1.55 $\mu\text{m}$  optical carrier will experience a serious dispersion distortion within a few km. To avoid this problem, optical-single-sideband transmission has been under investigation [15]. A simple alternative is to transmit the signal in baseband only and up-convert the baseband signal to the RF signal at the antenna site. This leads to the introduction of the following link configurations.

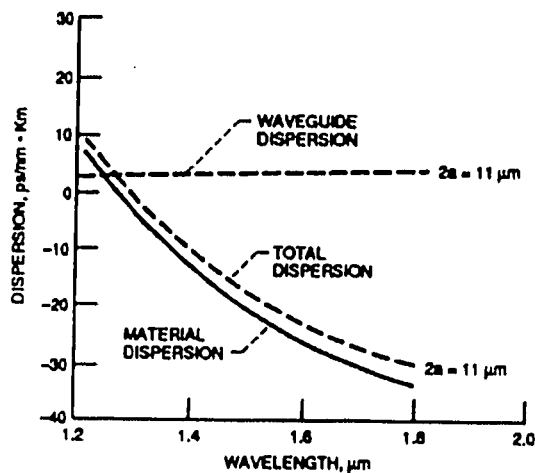


*FIG. 2 Magnitude of material and waveguide dispersion as a function of optical wavelength for a single-mode fused-silica-core fiber.[16]*

## 2.2 DM/DD fiber optic links with frequency up-conversion at the receiver site

To reduce the distortion due to the dispersion of the single mode fiber and to relax the requirement of high speed semiconductor laser, the data signal can be transmitted at baseband along the optical route and placed on the RF carrier at the antenna site. There are many ways to accomplish such frequency up-conversion.

### 2.2.1 using twin links

In this configuration, the data signal and the RF carrier reference are transmitted separately over different optical fibres as shown in FIG. 3. The performance of each link can be optimised for each particular frequency and bandwidth. The carrier reference can be generated using either high speed laser diodes/gas lasers or external optical modulators. For the downlink system where signals are transmitted from the central station to the remote antenna sites, this RF carrier reference can be shared by many links; therefore the overall cost is reduced. In addition, the up-converted system insertion loss can be reduced to minimum if a high gain data link and a carrier reference post detection amplifier are used. The major disadvantage is that it requires an additional optical fiber link. The total cost of the system will increase since a twice as much of fiber is needed. However, the high frequency RF carrier will suffer a serious dispersion distortion.

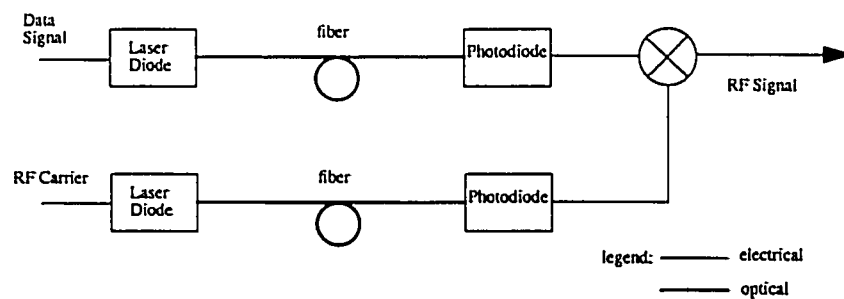


*FIG. 3 DM/DD using twin link*

### 2.2.2 using sub-harmonic injection technique

Instead of sending the RF carrier over a separate link directly, the RF carrier can be generated at the antenna site using sub-harmonic injection locked oscillator. Employing this technique can extend the length-bandwidth product of the link. There are two

types of optical injection-locking schemes: direct optical injection-locking [17][18] and indirect optical injection-locking [19].

Direct optical injection-locking

The schematic illustration of a direct optical injection-locking of a microwave oscillator is shown in FIG. 4. In this setup, the locking signal or the reference signal at frequency,  $f_1$ , is the sub-harmonic of  $f_o$ . Therefore, the sub-harmonic injection-locking technique allows the injection-locking of oscillators operating at a frequency much higher than the semiconductor laser relaxation frequency. For example, a 4 GHz reference signal can be sent to lock a 20 GHz RF carrier on 5<sup>th</sup> harmonic. The disadvantage of this locking technique is the difficulty of obtaining good coupling efficiency between the light signal beam and the narrow device active region. More efficient use of reference signal can be obtained by means of an induced optical system-locking scheme.

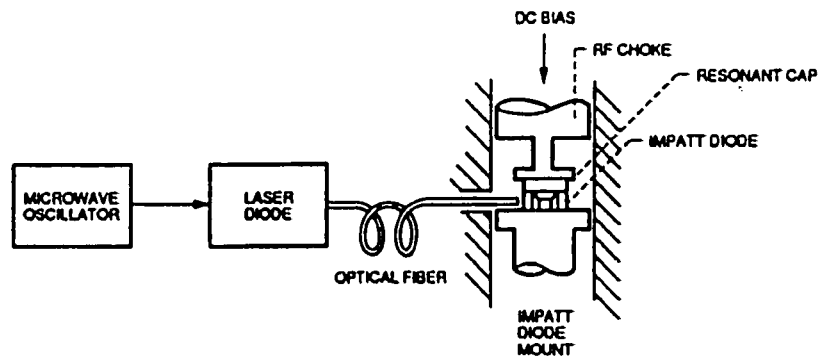


*FIG. 4 Schematic illustration of direct optical injection-locking technique of a CW IMPATT oscillator*

### Indirect optical injection-locking

The schematic illustration of the indirect optical injection-locking of a microwave oscillator is shown in FIG. 5. The locking signal or the reference signal at frequency  $f_1$  intensity modulates a laser diode operating at frequency  $f_c$ . The intensity-modulated optical signal is then detected by a photodetector and the detected signal is filtered, amplified and electrically injected into the oscillator.

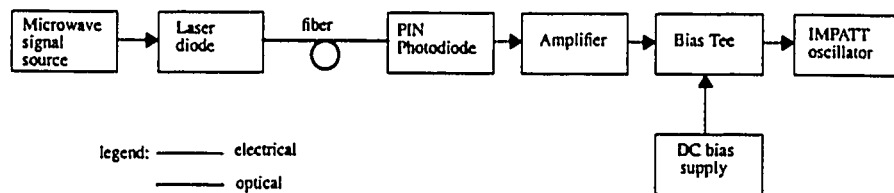


*FIG. 5 Schematic illustration of indirect optical injection-locking*

Herczfeld et al [19] demonstrate this technique using a silicon IMPATT oscillator. First, a 3.235 GHz tone intensity-modulates a laser diode. This modulation frequency happens to be close to the laser relaxation frequency so that the nonlinearity in the laser diode characteristic generates a large number of harmonics of the modulating signal. The intensity-modulated light output from the laser diode is then detected by a photodiode. The detected signal contains the original signal at 3.255 GHz as well as its harmonics. The fourth harmonic was selected by bandpass filtering, and then it was amplified and electrically injected through a bias tee to the biasing port of the free-running IMPATT oscillator. Injection-locking was observed at the third harmonics of the frequency of the injected electrical signal (i.e., at 38.820 GHz). Thus this injection-locking process occurred at the 12<sup>th</sup> harmonic with respect to the master signal. This



technique has the advantage of more efficient coupling of the laser light to the large-area photodiode than to the thin active region of the IMPATT diode as in the direct locking. However, the disadvantage of this technique is that it requires additional components that may increase the cost and the complexity of the circuit.

### 2.2.3 using frequency or wavelength division multiplexing

Instead of sending data and carrier reference over two fibres, they can be sent over a single fiber using frequency multiplexing. The link configuration is shown in FIG. 6.

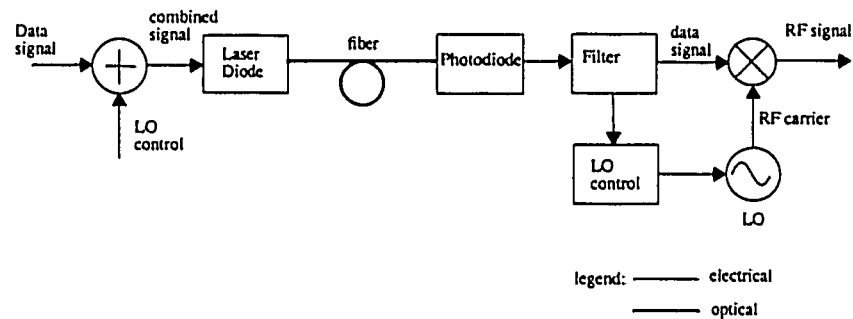


*FIG. 6 Frequency up-conversion using frequency multiplexing*

The data signal and the local oscillator control are combined by a power combiner and the combined signal intensity-modulates the output light intensity of the laser diode. At the receiver site, the combined signal is detected and then separated back into the data signal and the LO control using a pair of filters. The LO control injection-locks the LO to generate a RF carrier. Finally, the data signal is up-converted to the RF band by mixing with the RF carrier at a conventional microwave mixer. This configuration saves an optical fiber compared to the twin-links system but the system gain is lower. Although this configuration eliminates the need for high speed laser diodes and photodetectors, a microwave oscillator is required at each receiving site to generate the RF signal.

Another method is to use wavelength division multiplexing. The configuration is shown in FIG. 7.

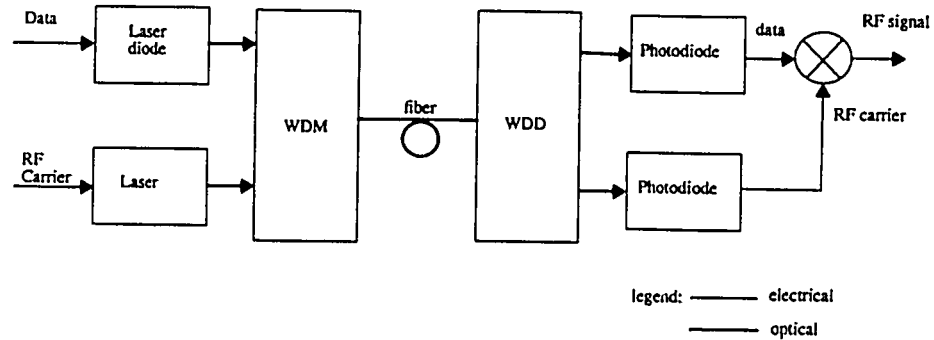


FIG. 7 Fiber optic link using WDM

### 2.2.4 using opto-electronic mixers (OEMs)

An OEM can replace the microwave mixer to upconvert the data signal to RF band. The link configuration is shown in FIG. 8.

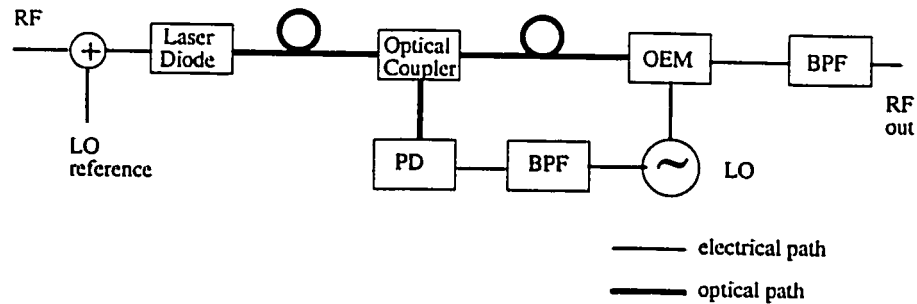


FIG. 8 Microwave fiber optic link using OEM

The operation at the transmitter side is the same as the previous configuration. At the receiver, the optical signal is divided into two routes by an optical coupler. Along the bottom route, the optical signal is detected by an inexpensive narrow band photore-

ceiver to select the RF carrier reference. Then the RF carrier reference is converted to an electrical signal and drives the OEM. Along the top route, the light is detected and mixed with the RF carrier reference. Mixing occurs because the responsivity of the OEM varies nonlinearly with the driving voltage. Finally, the electrical output containing the upconverted signal is amplified and radiated. The advantage of this link is the potential to reduce the size and the cost of the electrical transceivers by employing MMIC technology. Sub-harmonic injection-locking technique can also be used in this link.

### **2.3 Externally Modulated fiber optic links**

A typical schematic of an externally modulated link that consists of a semiconductor laser source, an external modulator, a photodiode and an optical fiber is shown in FIG. 9. In externally modulated links, the semiconductor lasers are operated in a dc mode; therefore, the signal does not experience frequency chirping that causes additional distortion. The linearity and the power consumption of the external modulator become the primary concerns when implementing this link configuration. The best performance, irrespective of the external modulator, is obtained when low-noise and high-power solid state lasers are incorporated, which can significantly lower the noise figure and increase gain and dynamic range. Millimetre wave subcarrier frequencies can be generated using a Mach-Zehnder interferometer. However, Mach-Zehnder interferometers are typically expensive and lossy.

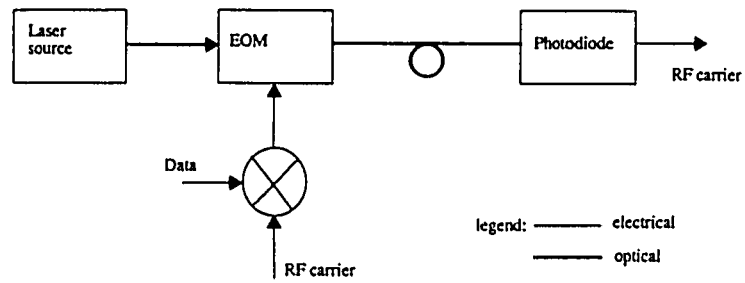


FIG. 9 External modulation link

## 2.4 Fiber optic mixing links

### 2.4.1 Dual mixing link

This configuration utilizes only one laser, one fiber and one detector to achieve millimetre wave transmission as shown in FIG. 10.

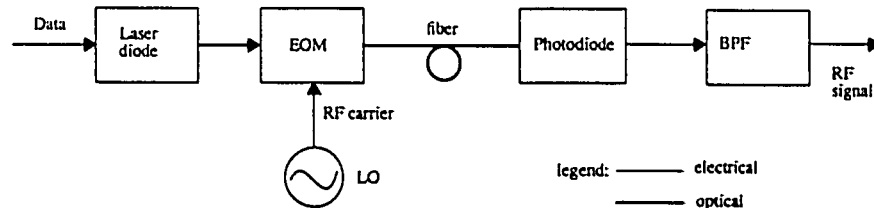
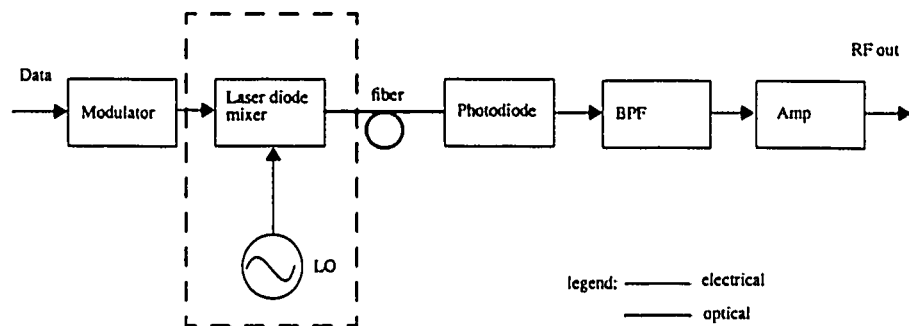


FIG. 10 Dual mixing link

In this configuration, the data signal directly intensity modulates the output light of the laser diode, and a single RF carrier signal is applied to the EOM. The EOM provides the mixing operation and the output of the EOM will contain the data signal, the RF carrier and their mixing products. It is easy to design this system with the data signal applied to the laser and the RF carrier applied to the EOM because this combination

will relax the high speed limitation of the laser. This configuration finds typical applications in high capacity wavelength multiplexing systems. This configuration reduces the complexity of the system. Although there is additional loss due to the insertion loss of the EOM, the performance does not greatly deteriorate if high power output lasers are used for the modulator source.

#### 2.4.2 Harmonic laser diode mixing link



*FIG. 11 Harmonic laser mixing link*

The configuration of this link is shown in FIG. 11. Although the laser diode can operate as an optical source and a microwave mixer simultaneously [5], the frequency of the transmitted millimetre wave is limited by the bandwidth of the laser diodes. The use of harmonics permits the modulation capability of the laser diode to be extended beyond the relaxation frequency limit. This allows better utilization of the fiber optic link bandwidth capability. The baseband data signal is supplied to the laser diode mixer. The laser diode is biased to produce high harmonic levels. The harmonics are used as the laser local oscillator signal for the laser mixer. The data signal and the microwave harmonics are mixed in the laser diode. The intensity modulated output of the laser diode contains the data signal, the laser harmonics and their mixing products. These

signals are transmitted to the receiver and are detected by the photodetector. The desired signal is selected by the BPF. The relationship between the output frequency,  $f_s$ , and the laser local oscillation frequency,  $f_l$ , is [6]:

$$f_s = M_l \cdot f_l \pm f_d \quad \text{EQ. 1}$$

where  $M_l$  is the harmonic of the local oscillator signal produced in the laser diode and  $f_d$  is the data signal frequency.

## 2.5 Proposed systems for analysis

We will analyse the CNR performance of three systems. The first one will employ the DM/DD link. Although this system will be expensive to realize due to the cost of high speed laser diodes, it can be used as a benchmark for the comparison. The second system will use a MSM PD as an OEM to up-convert the baseband signals to RF band signals. The system configuration is shown in FIG. 12. An injection locking technique is used to save the cost of a highly stable local oscillator.

The third system under investigation will use a loop configuration. This configuration reduces the amount of optical fiber cable that has to be installed to cover the service area compared to the star (point-to-point) configuration. The basic idea of the system is shown in FIG. 13. Starting and finishing at the central base station, each radio base station (RBS) is connected in series via two optical fibres.

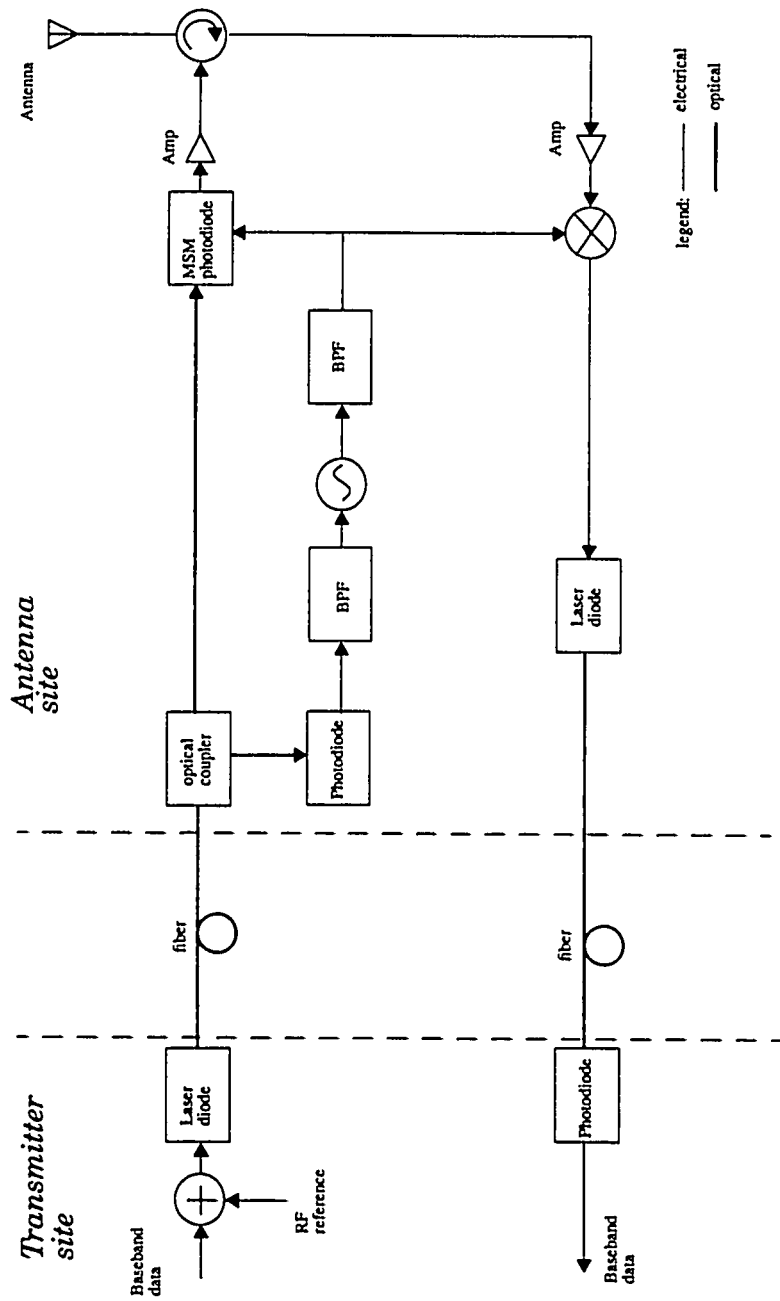


FIG. 12 DM/DD system using OEM

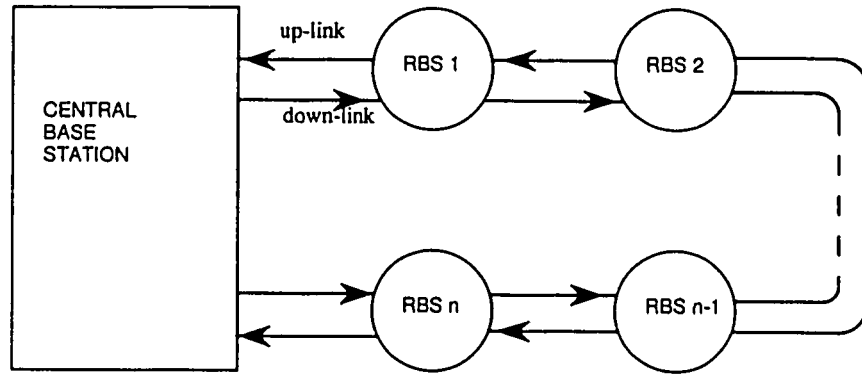


FIG. 13 Link configuration with cascaded radio base stations

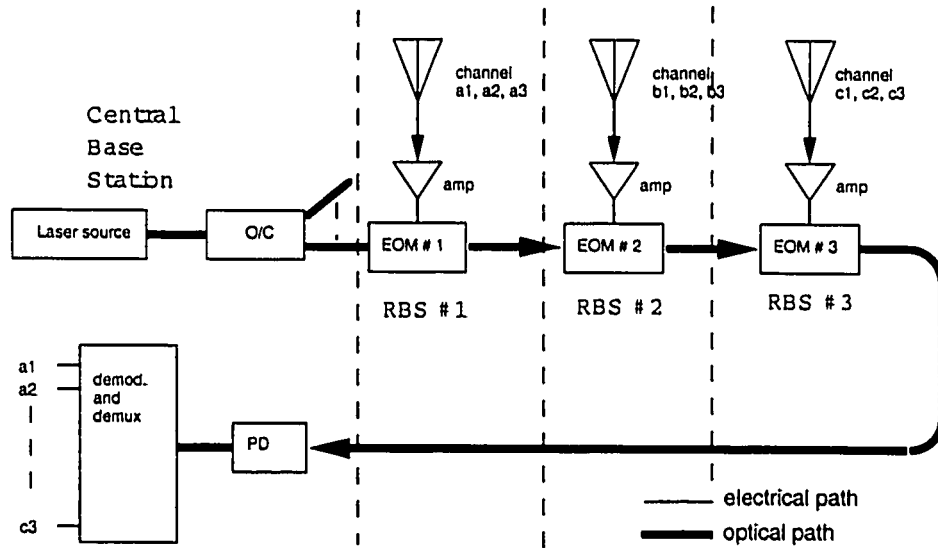


FIG. 14 Detailed configuration of the up-link system of the loop configuration

A detailed up-link configuration using cascaded external optical modulators (EOM) is shown in FIG. 14. The major components at the central base station (CBS) include a laser source, a photodiode, and a frequency demultiplexer. At each RBS, there is an antenna, an amplifier and an EOM for the up-link system. The single laser source in the CBS is used to provide continuous light to all the EOMs at the RBSs for modulation.



At each RBS, incoming radio signals are received by the antenna and then electrically amplified. These signals are then applied to the EOM and the intensity of the output light thus is modulated by the radio signal received by that RBS. At the end of the link, a photodetector is used to detect the signals. After the photodetector, a frequency demultiplexer is used to demultiplex the signals to their designated channels. Since a single laser source is used to supply continuous light to many RBSs, the cost for the laser source can be shared by these RBS; therefore, the average cost for the system can be reduced. Moreover, a higher power laser source can be used to distribute light to many links as shown in FIG. 14. to further reduce the overall cost.

A detailed down-link configuration is shown in FIG. 15. The major components at the CBS are a laser source, two EOMs, a local oscillator, a multiplexer and an encoder. The information signals are multiplexed and encoded using the designed modulation scheme. The laser source will generate a continuous light which will then be applied to the first EOM. At the first EOM, a RF carrier signal is applied to modulate the output light. At the second EOM, the encoded information signals are applied and they will mix with the RF subcarrier signal to produce up-converted signals. The output from the second EOM also contains the harmonics and the intermodulation products of both RF carrier and information signals. At each RBS, a portion of the light is coupled to the station using an optical coupler. Then a narrow-band photodetector will convert the optical signals at the selected frequency band into electrical signals, which will be amplified and radiated at the antenna.

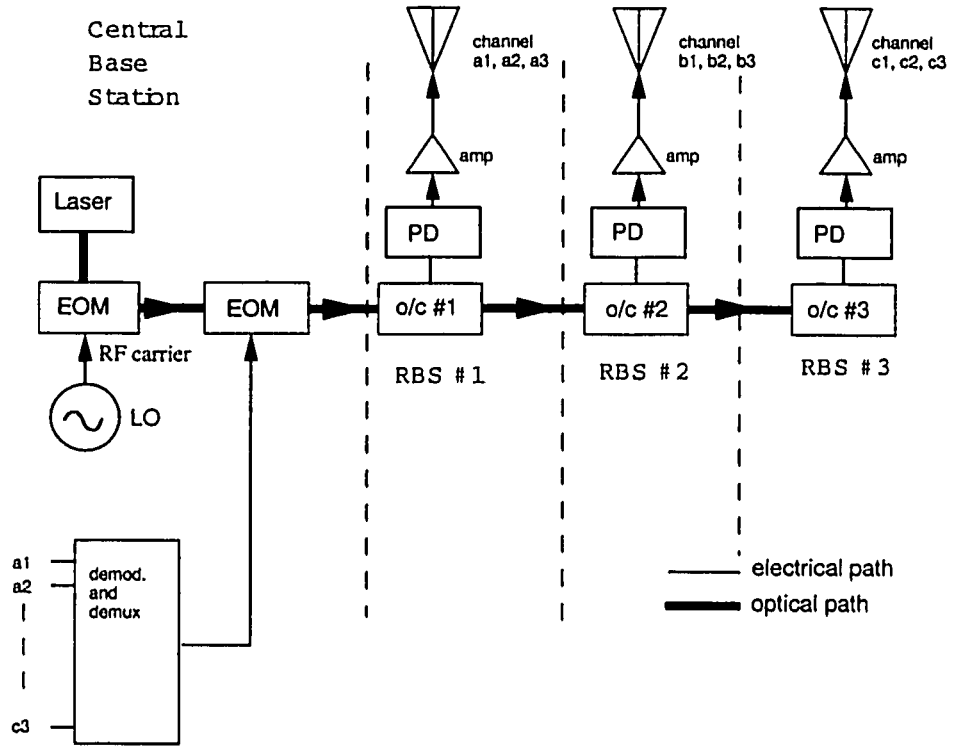


FIG. 15 Detailed configuration of the down-link system of the loop configuration

## 3.0 THEORY

This section presents the theoretical analysis of different components of a microwave fiber optic link. This includes laser diodes, external modulators, PIN photodiodes, and MSM photodetectors. The carrier-to-noise ratio analysis for the proposed systems is also presented.

### 3.1 Laser Diode

#### 3.1.1 The concept of stimulated emission

Three processes give rise to laser action: photon absorption, spontaneous emission, and stimulated emission. These three processes are illustrated in FIG. 16 by a simple two-level energy diagram. Plank's law states that a transition between two energy levels involves either the absorption or emission of a photon and this can be expressed mathematically as:

$$h\nu_{12} = E_2 - E_1 \quad \text{EQ. 2}$$

where  $E_2$  and  $E_1$  are the excite-state energy and the ground-state energy respectively,  $h\nu_{12}$  is the photon energy. In FIG. 16(a), an electron from the equilibrium energy state is excited to a higher energy state by the absorption of a photon of energy  $h\nu_{12}$ . Since this is an unstable state, the excited electron will return to the equilibrium state quickly, releasing the energy by emitting a photon of energy  $h\nu_{12}$  (FIG. 16(b)). This occurs without any external stimulation and is called spontaneous emission. These emission is isotropic and of random phase. When a photon of energy  $h\nu_{12}$  is incident while an electron is still at the excited state, the electron returns to the equilibrium state, emit-

ting a photon of energy  $h\nu_{12}$ . These emissions are in phase with the incident photon and this process is known as stimulated emission (FIG. 16(c)).

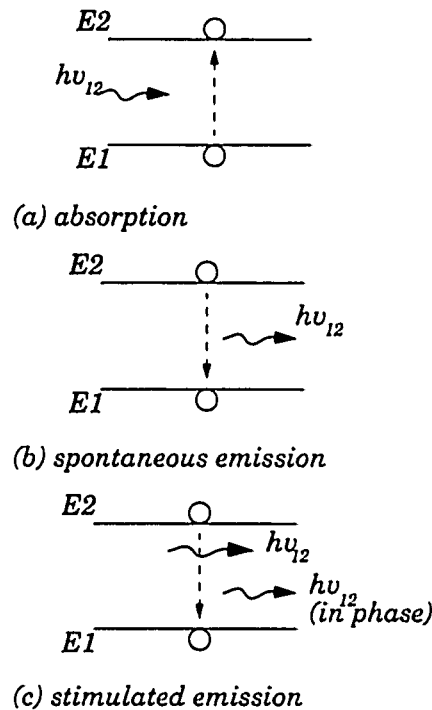


FIG. 16 The three vital transition processes in laser action.

When the systems are in thermal equilibrium, the density of excited electrons is very small; therefore, the systems will absorb most of the incident photons and there will be negligible stimulated emission. To enhance the stimulated emission, the population of the excited state electrons can be made larger than that of the equilibrium state by the process known as population inversion. In semiconductor laser, this is done by injecting electrons into the material at the device contact (DC biasing), filling the lower energy states of the conduction band.

### 3.1.2 Direct current modulation of semiconductor lasers

A typical plot of the output light power versus input current of a semiconductor laser is shown in FIG. 17. when the diode current is below the threshold, the laser diode operates in the spontaneous emission mode. When the diode current is increased from low current densities to high current densities in excess of the threshold, the light output from the laser increases and changes from spontaneous to stimulated emission. The most accurate method to model the laser diode characteristic will be one using the rate equations. However, the simulation time for the system performance analysis employing this approach is excessive. There is an abrupt transition in the slope of the transfer curve. It is very difficult to model the abrupt transition with just one polynomial function, and such modelling of the transfer characteristics could be inaccurate. To solve this, another approach to model the transfer curve is investigated. If only small signals are applied to the laser diode and it is biased so that it operates at the middle of the stimulated emission part of the transfer curve, we can find a polynomial approximation to the rate equation solution for the stimulated emission part only. Modelling of the spontaneous emission is not included in this approach.

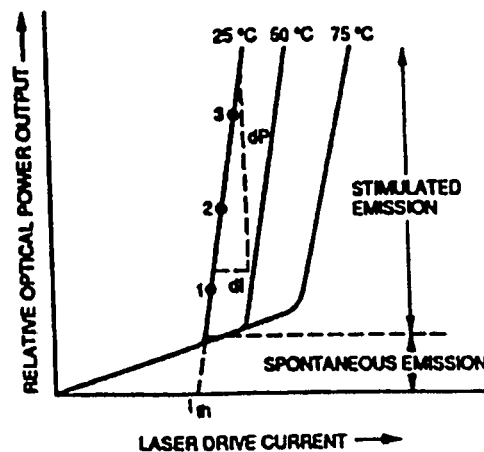


FIG. 17 Output light versus input diode current

The dynamic characteristics of semiconductor lasers can be described by a pair of rate equations shown as follows [20]:

$$\frac{dN}{dt} = - \sum_{i=-N_m}^{N_m} \frac{g_{oi}(N-N_t)S_i}{1 + \sum_{i=-N_m}^{N_m} \epsilon S_i} + \frac{I}{qV} - \frac{N}{\tau_n} \quad \text{EQ. 3}$$

$$\frac{dS}{dt} = \frac{\Gamma g_{oi}(N-N_t)S_i}{1 + \sum_{i=-N_m}^{N_m} \epsilon S_i} - \frac{S_i}{\tau_p} + \frac{\beta \Gamma N}{\tau_n} \quad \text{EQ. 4}$$

where  $N_m$  is the number of modes,  $N$  and  $S$  are the electron and photon densities,  $g_o$  is the differential gain,  $N_t$  is the carrier density for transparency,  $\tau_n$  and  $\tau_p$  are the spontaneous electron and photon lifetime, respectively,  $\Gamma$  is the optical confinement factor,  $\epsilon$  is a parameter characterizing the nonlinear gain,  $\beta$  is the fraction of spontaneous emission coupled into the lasing mode,  $I$  is the current through the active layer,  $q$  is the electron charge, and  $V$  is the volume of the active layer. If we assume that only a single lateral mode is present and the waveguide is less than a diffusion length wide, so that the lateral variations in the carrier density can be neglected, carrier diffusion can be ignored, and the laterally varying optical mode can be represented as a uniform photon density  $S$  with a time independent and space independent confinement factor,  $\Gamma$ . A similar assumption for the transverse (vertical) direction is also made. The cavity is assumed to be uniform with two reflecting facets. Moreover, the current injection is uniform and the mirror loss is small enough compared to the internal loss that the carrier and photon variations along the laser length can be ignored. With the above assumptions, equation 1 and 2 can be simplified as follows [21]:

$$\frac{dN}{dt} = -\frac{g_o(N-N_t)S}{1+\epsilon S} + \frac{I}{qV} - \frac{N}{\tau_n} \quad \text{EQ. 5}$$

$$\frac{dS}{dt} = -\frac{\Gamma g_o(N-N_t)S}{1+\epsilon S} - \frac{S}{\tau_p} + \frac{\beta\Gamma N}{\tau_n} \quad \text{EQ. 6}$$

Experimental measurements have found the following empirical relationship between the threshold current  $I_{th}$  and temperature [22]:

$$I_{th}(T) = I_c \exp\left(\frac{T}{T_o}\right) \quad \text{EQ. 7}$$

where  $I_c$  is the current constant,  $T_o$  is the characteristic temperature of the diode, and  $T$  is the temperature. To find a more accurate simulation of laser diodes, we have to relate this equation to the parameters of the rate equations. Many parameters of the rate equations such as  $\tau_n$  are temperature dependent; however this temperature dependence is implicitly contained within EQ. 7 [23]. Therefore, the temperature dependent parameters considered for EQ. 5 and EQ. 6 are [23]:

$$g_o(T) = g_{co} \exp\left(\frac{-T}{T_{oa}}\right) \quad \text{EQ. 8}$$

and

$$N_t(T) = N_{ct} \exp\left(\frac{T}{T_{oa}}\right) \quad \text{EQ. 9}$$

where  $T_{oa}$  is the characteristic temperature for the active region. We use EQ. 5 to EQ. 9 to derive the output optical power versus input injection current transfer characteristic of laser diodes. The complete derivation is shown in Appendix A, and the final expression is as follows:

$$0 = aS^2 + bS + c \quad \text{EQ. 10}$$

where

$$a = \frac{g_o}{\tau_p} + \frac{\epsilon}{\tau_n \tau_p},$$

$$b = \frac{\Gamma g_o N_t}{\tau_n} + \frac{1}{\tau_n \tau_p} - \frac{\Gamma g_o I_o}{qV} - \frac{\beta \Gamma I_o \epsilon}{qV \tau_n} - \frac{\beta \Gamma g_o N_t}{\tau_n},$$

$$c = -\frac{\beta \Gamma I_o}{qV \tau_n},$$

where  $I_o$  is the applied dc current. The transfer characteristic can be obtained by solving for  $S$  in the Eqn 10. After plotting the curve, the stimulated emission portion of the transfer characteristic curve (the more linear part) can be modelled by a polynomial function. We use a curve fitting method to model the curve as a third-order polynomial function as follows:

$$P = a_3 I^3 + a_2 I^2 + a_1 I + a_0. \quad \text{EQ. 11}$$

A third-order polynomial is chosen because the third order term  $I^3$  contributes to the third order intermodulation products. Intermodulation distortion will be explained in the later section.



The plot of the output light power versus the input diode current transfer characteristics is shown in FIG. 18.

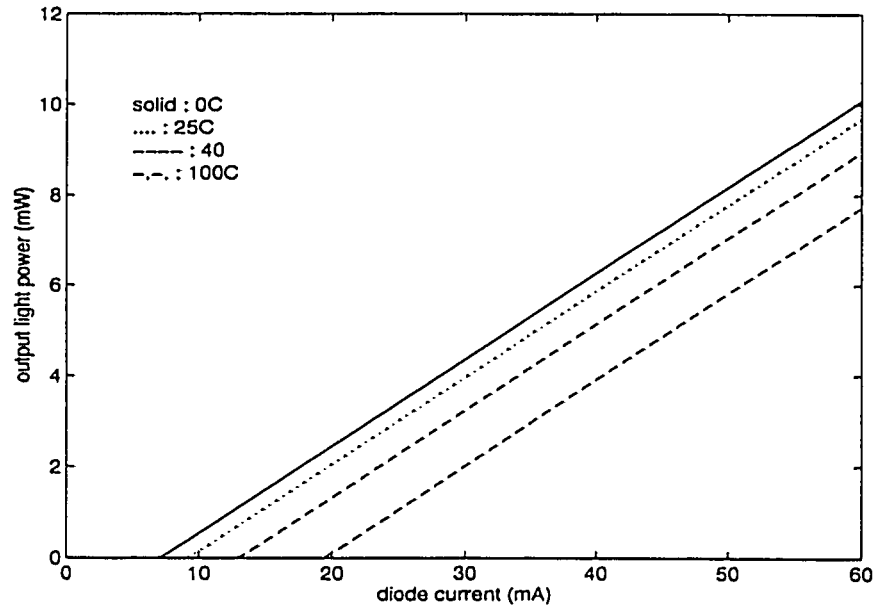


FIG. 18 Output Light versus Diode Current

From FIG. 18, we see that the threshold current increases with temperature. This agrees with the experimental results. The parameters used for the calculation of results in FIG. 18 are listed in TABLE 1..

Name	Description	Value	Unit
$V$	active volume of laser cavity	$0.8427 \times 10^{-16}$	$m^3$
$\beta$	fraction of spontaneous emission coupled into lasing mode	$1 \times 10^{-4}$	
$\Gamma$	optical confinement factor	0.4	
$\epsilon$	gain factor	$2.0 \times 10^{-23}$	$m^3$
$q$	electron charge	$1.6 \times 10^{-19}$	C
$\tau_n$	spontaneous recombination time	$3 \times 10^{-9}$	s
$\tau_p$	photon lifetime	$0.7 \times 10^{-12}$	s

TABLE 1. Parameters used for calculating the transfer characteristics of laser diodes

Name	Description	Value	Unit
$N_t$	transparency electron density	$0.59 \times 10^{23}$	$m^{-3}$
$g_{co}$	gain constant	$8.0 \times 10^{-11}$	$m^3 s^{-1}$

TABLE 1. Parameters used for calculating the transfer characteristics of laser diodes

Now we use the curve fitting method as explained in section 2 to find the coefficients of the polynomial that will model the stimulated emission part of the transfer characteristic of the laser diode. The results are summarized in TABLE 2..

Temp (C)	$a_3$ (mW/mA <sup>3</sup> )	$a_2$ (mW/mA <sup>2</sup> )	$a_1$ (mW/mA)	$a_0$ (mW)
0	-0.0015	0.0002	0.1909	-0.0014
25	-0.0018	0.0002	0.1908	-0.0017
40	-0.0025	0.0003	0.1908	-0.0020
60	-0.0039	0.0006	0.1907	-0.0025
80	-0.0069	0.0010	0.1905	-0.0030
100	-0.0159	0.0024	0.1904	-0.0037

TABLE 2. Coefficients at different temperature

From TABLE 2., we can see that the coefficients  $a_3$  increases with the temperature. This term contributes to the 3IMD. Therefore the 3IMD has a larger effect at the higher temperatures. After obtaining the coefficients of the polynomial, we can proceed to calculate the CNR performance of the microwave fiber optic links.

### 3.2 External Modulator

The Mach-Zehnder interferometer is a popular optical external modulator. The principle of the Mach-Zehnder interferometer is based on the electro-optic properties of some special material such as lithium nobate (LiNbO<sub>3</sub>). When an electric field is applied to such material, its refractive index changes. Lithium nobate is a common material used for Mach-Zehnders because of its high electro-optic coefficients. The

variation of the refractive index of a material with high electro-optic coefficient is more sensitive to the change of the applied electric field.

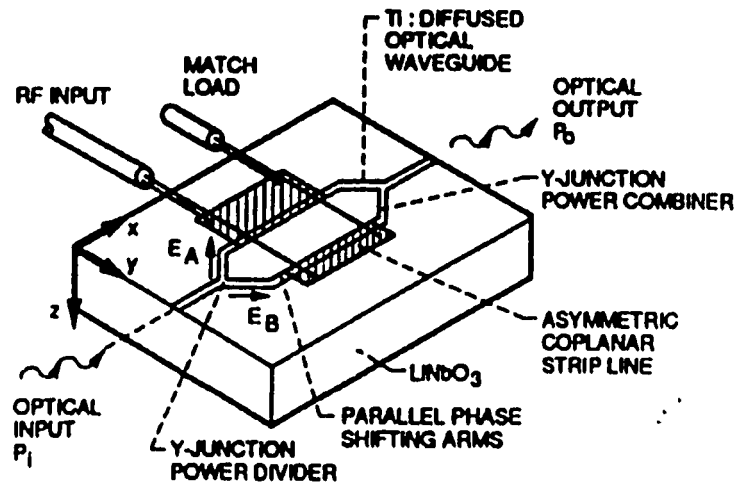


FIG. 19 Structure of a Mach-Zehnder modulator

The basic structure of a Mach-Zehnder is shown in FIG. 19. When light enters the device, it is divided equally at the first Y-junction into two arms. A pair of electrodes are placed on the two parallel arms where the RF drive voltages are applied. The guided light propagating along the top arm undergoes a phase shift and interferes with the other light propagating along the bottom arm at the output Y-junction. The combined output light intensity is thus modulated in response to the phase difference between these two guided light beams.

The transmittance of a Mach-Zehnder can be expressed as:

$$T(V) = \frac{1}{2} \cdot \left( 1 + \cos \left( \phi_o + \frac{\pi \cdot V}{V_\pi} \right) \right) \quad \text{EQ. 12}$$

where  $\phi_o$  is the bias point,  $V$  is the applied voltage, and  $V_\pi$  is the half wave voltage. A simple plot of EQ. 12 is shown in FIG. 20.

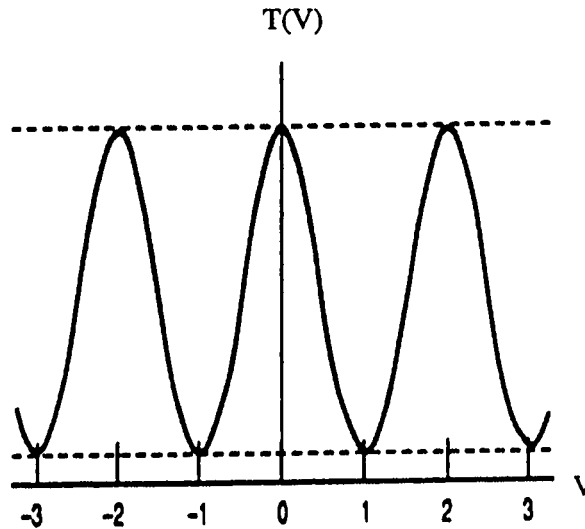


*FIG. 20 Transfer characteristics of an EOM*

### **3.3 Photodetector**

#### **3.3.1 PIN photodiode**

A PIN photodiode consists of a p-type and a n-type semiconductor region separated by an intrinsic layer. The structure diagram of a PIN photodiode is shown in FIG. 21. In normal operation, a sufficiently large reverse bias voltage is applied across the device so that the intrinsic region is fully depleted of carriers. This reverse bias sets up an electric field equal to the saturation field so that the carriers travel at the saturation velocity during most of the transition. When a photon of energy equal to or greater than the semiconductor bandgap energy is incident, the energy of the photon is absorbed

and an electron is excited from the valence band to the conduction band. Therefore, free electron-hole pairs are generated and they are known as photocarriers. Photodiodes are normally designed so that most of the photocarriers are generated in the depletion region where most of the light is absorbed. The high electric field present in the depletion region forces the photocarriers to be separated and collected across the reverse biased junction. As the carriers traverse the depletion region, a displacement current known as photocurrent is induced.

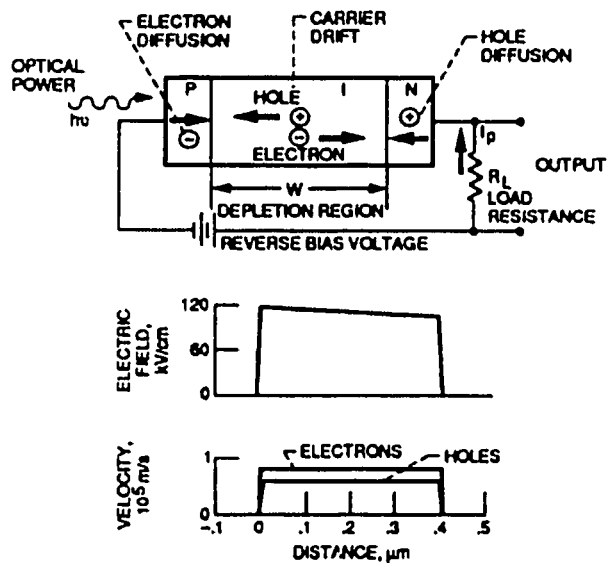


*FIG. 21 Schematic representation of a reverse-biased one-dimensional PIN photodiode*

Photodiodes are characterised by two parameters: quantum efficiency and responsivity. Quantum efficiency,  $\eta$ , is defined as the ratio of the number of photo-electrons collected at the detector terminal to the number of photons incident on the photodiode.

Responsivity,  $R$ , is used to characterize the performance of a photodetector and it is defined as:

$$R = \frac{I_p}{P_o} \quad \text{EQ. 13}$$

where  $I_p$  is the output photocurrent and  $P_o$  is the incident optical power. The unit for responsivity is A/W. Responsivity is a useful parameter as it gives the transfer characteristic of the detector.

### 3.3.2 MSM photodetector

In addition to the detection of the incident light, metal-semiconductor-metal (MSM) photodiodes can perform frequency conversion as well. Their high bandwidth, simple planar structure, very low capacitance and monolithic integrability with FETs make them very attractive over other photodetector mixers such as avalanche photodiodes (APD) and phototransistor optoelectronic mixers.

The frequency conversion process is possible at the MSM photodiode because the responsivity of the MSM PD can be controlled by the applied voltage [24]. The responsivity of the MSM PD also depends on the wavelength of operation, the size of the device's active area, finger width, length, etc [25]. The output photocurrent of the MSM PD is given by

$$I_{ph}(t) = K[V(t)] \cdot P(t) \quad \text{EQ. 14}$$

where  $P(t)$  is the optical power of the incident intensity modulated signal,  $K[V(t)]$  is the responsivity of the MSM PD as a function of the LO voltage  $V(t)$  applied with the bias. The photocurrent generated at the output of the MSM PD contains the original

signal, LO signal, harmonics, intermodulation, and the mixing products. The desired signal can be selected by filtering.

To understand the mixing behaviour of the MSM PD better, the dc responsivity,  $R_{V_{dc}}$ , is modelled as an analytical function in terms of the applied voltage:

$$R_{V_{dc}} = \left( A_0 + A_1 \cdot V_{dc} + A_2 \cdot V_{dc}^2 + A_3 \cdot V_{dc}^3 \right) \cdot \tanh(\alpha \cdot V_{dc}) \quad \text{EQ. 15}$$

where the constants  $A_0$ ,  $A_1$ ,  $A_2$ , and  $A_3$  are obtained from a curve fitting model of the experimental data and are listed in TABLE 1. The plot of EQ. 15 is shown in FIG. 22. The dc responsivity is linearly related to the bias at low biasing voltages. This may be because the carrier transit time is longer than the carrier lifetime. At high biasing voltages, the responsivity becomes independent of the applied voltage.

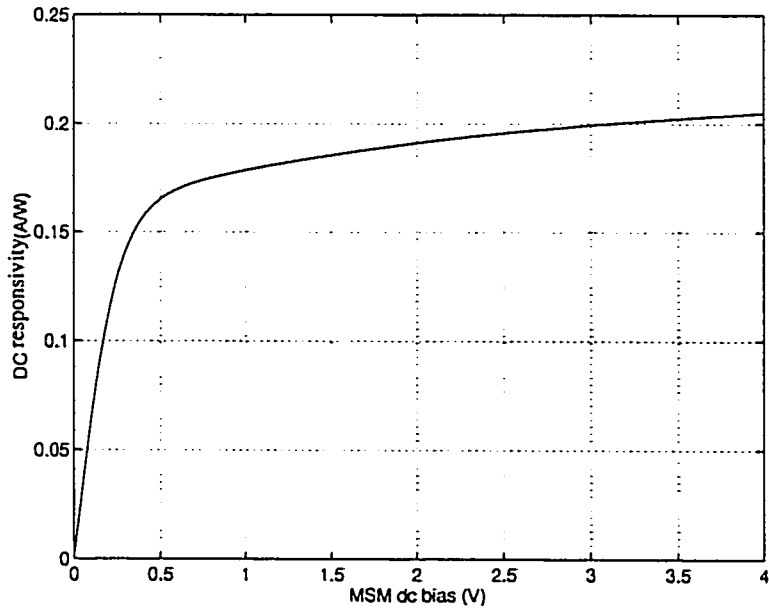


*FIG. 22 DC responsivity of the MSM PD*

When the MSM PD is used as a mixer, it is biased by a LO voltage  $V_{lo}$  and the resulting responsivity  $R$  can be modelled as:

$$R = \sum_{n=0}^N \{A_n (V_{dc} + V_{lo} \cos(\omega_{lo} t))\} \cdot \tanh[\alpha (V_{dc} + V_{lo} \cos(\omega_{lo} t))] \quad \text{EQ. 16}$$

where  $N=3$  gives a good agreement with the measured results. After the series expansion of EQ. 16, the responsivity can be expressed in terms of the LO frequency component and its harmonics as follows [26]:

$$R = K_0 + K_1 \cos(\omega_{lo} t) + K_2 \cos(2\omega_{lo} t) + K_3 \cos(3\omega_{lo} t) \quad \text{EQ. 17}$$

where

$$K_0 = A_3 V_{dc}^3 + A_2 V_{dc}^2 + \left(A_1 + \frac{3}{2} A_3 V_{lo}^2\right) V_{dc} + A_0 + \frac{A_2 V_{lo}^2}{2},$$

$$K_1 = 3A_3 V_{lo} V_{dc}^2 + 2A_2 V_{lo} V_{dc} + \frac{3}{4} A_3 V_{lo}^3 + A_1 V_{lo},$$

$$K_2 = \frac{3}{2} A_3 V_{dc} V_{lo}^2 + \frac{1}{2} A_2 V_{lo}^2,$$

$$K_3 = \frac{1}{4} A_3 V_{lo}^3.$$

## 3.4 Noise

### 3.4.1 Thermal noise

Thermal noise is associated with the bias resistor in the photodetector circuit and is due to the spontaneous fluctuations of the currents or voltages in the bias circuit. The mean square value of this noise current in a noise equivalent bandwidth  $B$  is given by



$$\langle I_{th}^2 \rangle = \frac{4kTB}{R_b} \quad \text{EQ. 18}$$

where  $k$  is the Boltzmann's constant,  $T$  is the absolute temperature and  $R_b$  is the bias resistance.

### 3.4.2 Shot noise

Shot noise is a result of the random arrival of the signal photons and also the dark current in the detector. When there is no optical power incident on the photodetector, a small reverse leakage current still flows from the device terminal. This current is known as the dark current. It is proportional to the total detected photocurrent. The mean square shot noise current is given by

$$\langle I_{sh}^2 \rangle = 2qR\beta P_0 B = 2qI_{dc} B \quad \text{EQ. 19}$$

where  $\beta$  is the link loss,  $P_0$  is the optical power at the laser output and  $q$  is the electronic charge.

### 3.4.3 Relative intensity noise

The apparent intensity noise at the receiver consists of noise intrinsic to the laser due to quantum effects in electron to photon conversion, mode partitioning, and extrinsic effects such as reflection, scattering and dispersion. Reflection effects are more predominant when highly stabilized lasers are used in the long wavelength windows. The mean square value of the equivalent intensity noise current is given by

$$\langle I_{RIN}^2 \rangle = RIN \cdot I_{dc}^2 \cdot B \quad \text{EQ. 20}$$

where RIN is the relative intensity noise factor which takes into account the overall noise variation that occur at the transmitter end.

#### **3.4.4 Intermodulation noise**

The nonlinearity characteristics of a component such as the laser diode in the fiber optic link can generate higher harmonics distortion signals as well as second and third order intermodulation (IMD) products. IMD products result when two closely spaced subcarriers  $f_1$  and  $f_2$  pass to the nonlinear device. The most important contributions to this noise results from the third order IMD products. The second order IMD products fall outside the information bandwidth and can be eliminated by some bandpass filters. However, the third order IMD products fall into the information bandwidth and they cannot be removed by filters. IMD noise greatly reduces the dynamic range of the link. The expressions for this noise are different from system to system and they will be covered in the next section. The relationship of the signals and their third intermodulation products is shown in FIG. 23.

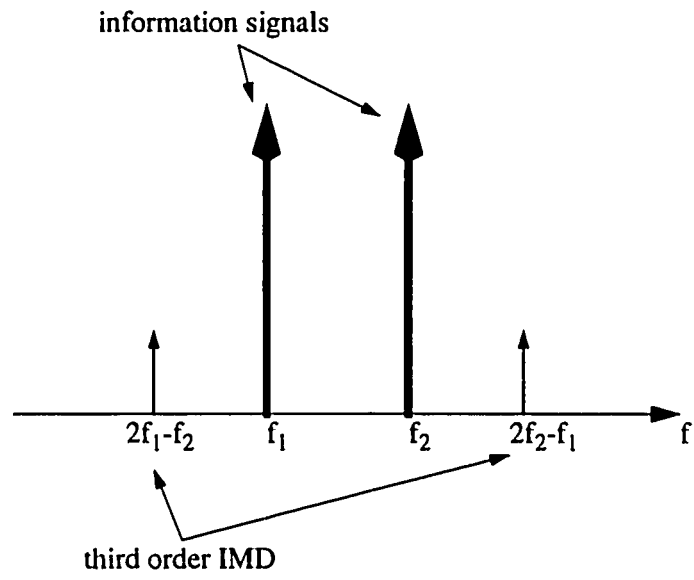


*FIG. 23 Relationship of signals and IMD*

## 4.0 PROPOSED SYSTEMS PERFORMANCE ANALYSIS

### 4.1 DM/DD

If we bias the laser diode at the middle of the lasing region and drive it with a small signal, the output light power versus input diode current transfer characteristic can be expressed as a Taylor series about  $I_o$  as follows [27]:

$$P = c_0 + c_1 (I_a - I_o) + c_2 (I_a - I_o)^2 + c_3 (I_a - I_o)^3 + \dots \quad \text{EQ. 21}$$

where  $c_0$ ,  $c_1$ ,  $c_2$ , and  $c_3$  are the transfer coefficients.  $I_a$  is the applied current and is expressed as follows:

$$I_a = I_o + \sum_{n=1}^N I_n \cos(\omega_n t) \quad \text{EQ. 22}$$

where  $I_o$  is the dc current,  $I_n$  is the peak signal current of channel  $n$ ,  $N$  is the number

of channels. Letting  $i = \sum_{n=1}^N I_n \cos(\omega_n t)$  and rearranging EQ. 21, we obtain the final

expression as follows:

$$P = P_o \left( 1 + a_1 I + a_2 I^2 + a_3 I^3 + \dots \right) \quad \text{EQ. 23}$$

where

$$a_1 = c_1,$$

$$a_2 = P_o c_2,$$

$$a_3 = P_o^2 c_3,$$

$$I = \sum_{i=1}^N m_i \cos(\omega_i t),$$

and  $m_i$  is defined as  $\frac{I_i}{P_o}$ . The complete derivation is shown in the Appendix B. The fourth term of EQ. 23 contains many third order intermodulation products that fall into the information band. These intermodulation products cannot be removed by bandpass filtering and are known as third order intermodulation distortion (3IMD). This noise will degrade the carrier-to-noise ratio (CNR) of the link. Other noises present in the link include the relative intensity noise for the laser diode, shot noise and thermal noise. The carrier to noise ratio of a direct modulation link can be expressed as follows [28]:

$$CNR = \frac{\frac{1}{2} m^2 I_{ph}^2}{\left( RIN \cdot I_{ph}^2 + 2qI_{ph} + \langle I_{th}^2 \rangle \right) BW + IMD} \quad \text{EQ. 24}$$

where BW is the bandwidth per carrier (channel), RIN is the relative intensity noise for the laser diode at the transmitter, m is the modulation index, IMD is the total intermodulation distortion power,  $\langle I_{th}^2 \rangle$  is the equivalent input noise current density in the optical receiver,  $I_{ph}$  is the average received current:

$$I_{ph} = \eta \frac{P_o}{L} \quad \text{EQ. 25}$$

where  $\eta$  is the photodiode sensitivity, L is the fiber loss including the connector loss.

As the number of carriers (channels) increases, the interference from the 3IMD also increases. There are two types of 3IMD, a two-tone type and a three-tone type. A two-

tone type 3IMD occurs by the combination of two RF signals while a three-tone type occurs by the combination of three RF signals. If we assume that  $n$  carriers are separated by equal interval on the frequency axis, the number of two-tone type 3IMD, called  $D_2(n, r)$ , and that of three-tone type 3IMD, called  $D_3(n, r)$ , influenced on the  $r^{th}$  carrier of  $n$  carriers, are given as follows [29]:

$$D_2(n, r) = \frac{1}{2} \left[ n - 2 + \frac{1}{2} \{1 - (-1)^n\} \{-1\}^r \right] \quad \text{EQ. 26}$$

$$D_3(n, r) = \frac{r}{2} (n - r + 1) + \frac{1}{4} \{ (n - 3)^2 - 5 \} - \frac{1}{8} \{1 - (-1)^n\} \{-1\}^{n+r}. \quad \text{EQ. 27}$$

We assume that the modulation indexes are the same for all channels, and the amplitudes of the two-tone 3IMD and the three-tone 3IMD are given as:

$$\frac{3}{4} a_3 m^3 : \text{two-tone type;}$$

$$\frac{3}{2} a_3 m^3 : \text{three-tone type.}$$

Finally, the amount of 3IMD in the  $r^{th}$  carrier of  $n$  carriers is given as [28]:

$$IMD = \frac{1}{2} \left( \frac{3}{4} a_3 m^3 D_2(n, r) + \frac{3}{2} a_3 m^3 D_3(n, r) \right)^2 I_{ph}^2 \quad \text{EQ. 28}$$

Since the center carrier of the  $n$  carriers suffers the largest IMD, the CNR of the center carrier is the worst. As a result, we consider the center channel in our analysis for the worst case.

The CNR performance of the link for different parameters are shown in the following figures. The parameters used in the calculation is listed in TABLE 3. From EQ. 24, we

can see that the signal power is proportional to  $m^2$  while the power of the IMD is proportional to  $m^6$ , therefore, the carrier to intermodulation ratio is  $1/m^4$ . This implies that when the optical modulation index is small, the degradation due to intermodulation distortion is small and may be negligible, and the major noise sources of the link will be the thermal noise and the shot noise. When  $m$  increases, the CNR improves. However, the CNR will increase to a maximum point and then the IMD starts to dominate. After that point, the CNR starts to degrade due to the rapid increase of the power of IMD. As a result, there is an optimal modulation index that gives the highest CNR. For example, for a 20 channel system, the highest CNR is 65 dB when the OMI is -30 dB at 0 °C. From FIG. 25, we can see that the peak CNR occurs at a lower OMI than in FIG. 24. The peak CNR also has a lower value than in FIG. 24. This is because when the operating temperature increases, the coefficient  $a_3$  (the third order coefficient of the laser diode transfer characteristic polynomial) increases. This will contribute a larger IMD, thus IMD starts to dominate at a lower OMI. We also see that the CNR degrades when the number of channels increases. Since the number of IMD products is proportional to the number of channels, the power of the IMD is also proportional to the number of channels. As a result, the system with more channels suffers larger IMD and CNR degrades. The above parameters contribute noise due to IMD; therefore at lower OMI, the CNRs are the same for the links with different parameters. However, the increase of the channel bandwidth (BW) enhances the contribution from the other sources of noise, i.e. RIN, thermal, and shot noise. We can see that, in FIG. 27, at lower OMI, the CNRs are different for the links with different BW, but at the higher OMI, the IMD is dominant and the CNRs are the same for the links with different BW. From EQ. 23, we can see that the RIN, thermal noise and shot noise are proportional to BW; therefore, as the channel BW increases, noise increases and CNR decreases. For exam-

ple, the link with 30 kHz channel BW has a 10 dB improvement on CNR compared to the link with 1 MHz channel BW.

Name	Value	Unit
laser output power	0	dBm
fiber loss (include connector loss)	2	dB
RIN	-152	db/Hz
BW	30	Hz
detector sensitivity	0.8	A/W
Vdc	2	V
Vlo	1	V

TABLE 3. Parameters used to calculate CNR

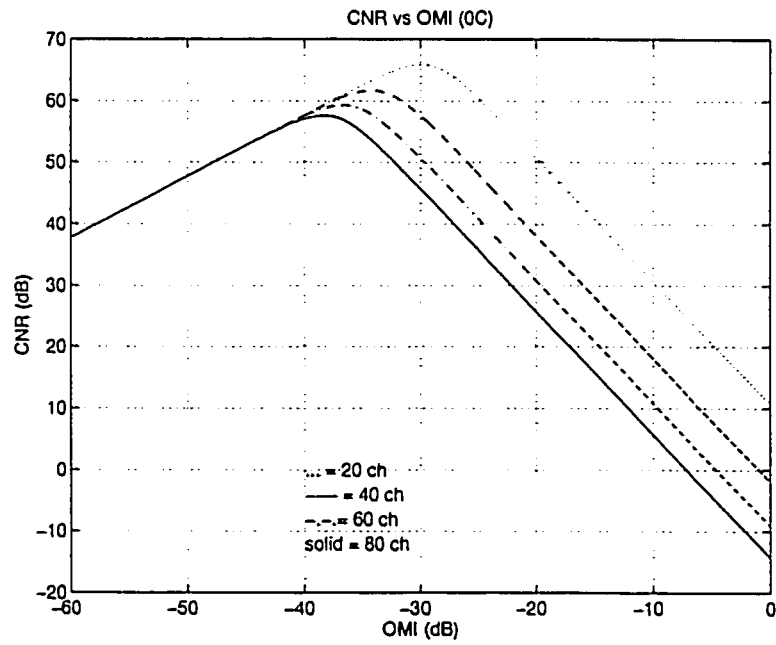
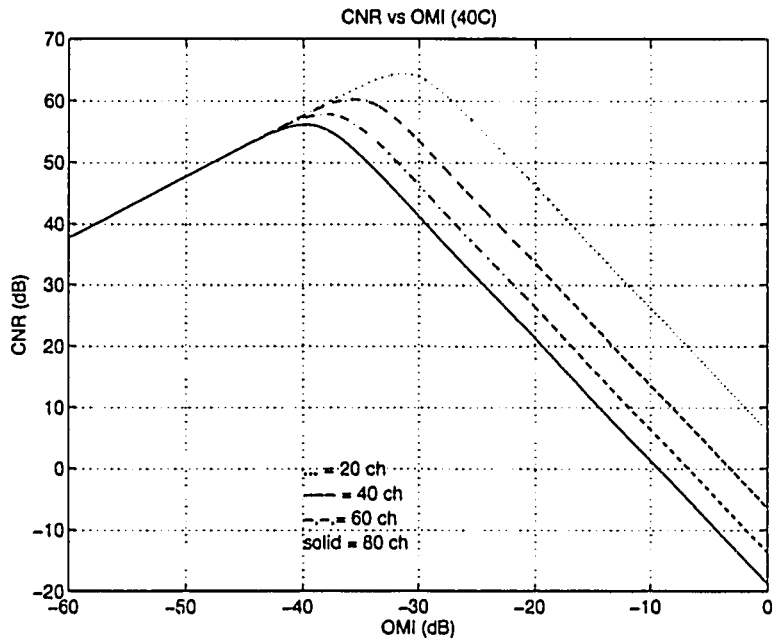
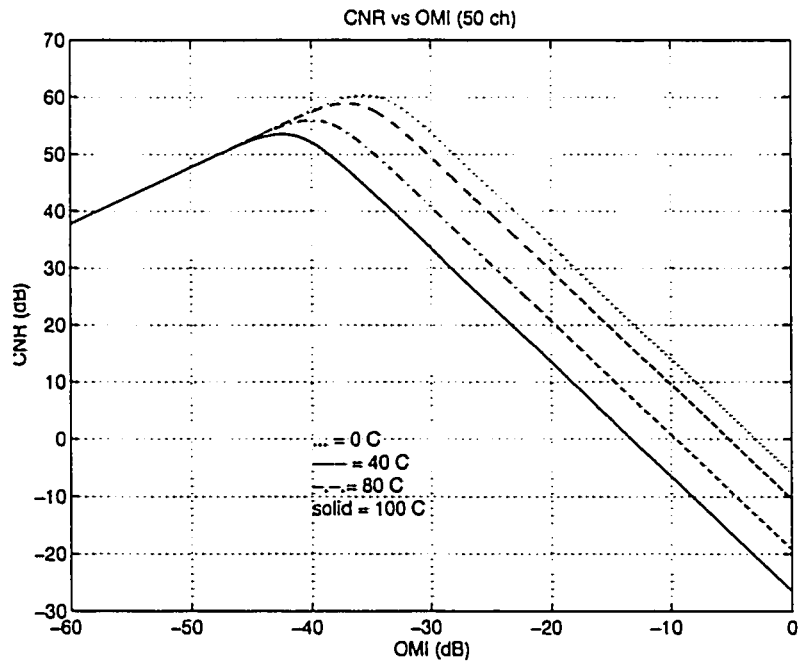


FIG. 24 CNR performance of the DM/DD link at 0 °C





*FIG. 25 CNR performance of the DM/DD link at 40 °C*



*FIG. 26 CNR performance of the DM/DD link with temperature as a parameter*

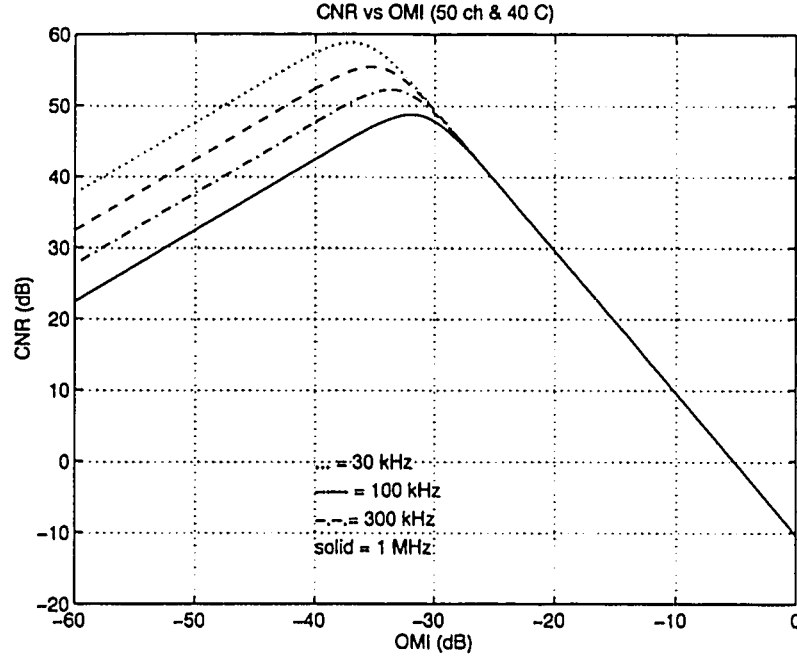


FIG. 27 CNR performance of the DM/DD link with channel BW as a parameter

## 4.2 DM/DD using an OEM

The analysis of this link is the same as the DM/DD link except for the receiver site. At the receiver, an MSM PD is used to detect the signal and simultaneously performs the frequency conversion. From section 3.3.2, the responsivity is:

$$R = K_0 + K_1 \cos(\omega_{LO}t) + K_2 \cos(2\omega_{LO}t) + K_3 \cos(3\omega_{LO}t) \quad \text{EQ. 29}$$

where  $K_n$  ( $n=0,1,2,3$ ) are the MSM coefficients depending on  $A_n$ ,  $V_{dc}$ ,  $V_{LO}$  as presented in section 3. The CNR of such a link is:

$$CNR = \frac{\langle I_{up}^2 \rangle}{\left( RIN \cdot I_{dc}^2 + 2qI_{dc} + \langle I_{th}^2 \rangle \right) BW + IMD} \quad \text{EQ. 30}$$

where  $\langle I_{up}^2 \rangle$  is the up-converted signal and is as follows:

$$\langle I_{up}^2 \rangle = \frac{1}{8} m^2 P_f^2 K_1^2,$$

and  $I_{dc} = RP_f = R\eta P_o$ .

The CNR performance of this link is shown in FIG. 28. We see that the graph is very similar to those of the DM/DD link. The previous discussion of the performance of the DM/DD link also applies to this link. In general, the CNR of the link using OEM (link #1) is lower than the CNR of the link without OEM (link #2) using the same parameters. For example, at 0 °C, a 20 channels link #2 with 30 kHz channel BW has a peak CNR of 39 dB. This is about 29 dB lower than the link #1 with the same parameters. The degradation of CNR is because of the conversion loss and insertion loss of the MSM photodiodes. However, we should expect a 3 to 5 dB degradation of CNR in link #1 if we include the penalty of the frequency conversion procedure using a conventional microwave mixer. Although the CNR of link #2 is lower, it has the potential of reducing the size and the cost of electrical transceivers by employing MMIC technology. We also find that the CNR peak in link #2 occurs at much higher OMI. This results from the higher thermal noise and shot noise. These noise dominates at higher OMI, thus the peak CNR occurs at higher OMI. Improvement of the component quality may improve the CNR.

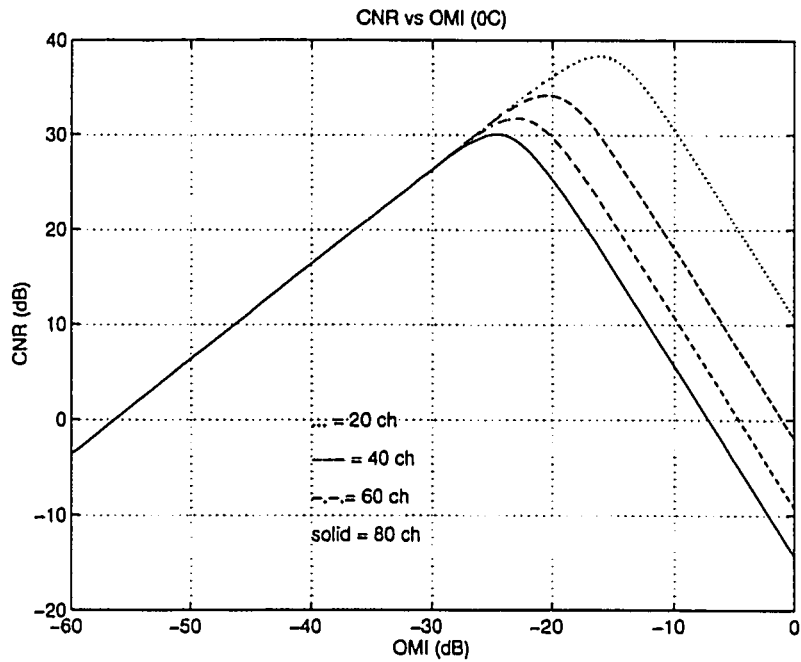


*FIG. 28 CNR of the DM/DD link using OEM at 0 °C*

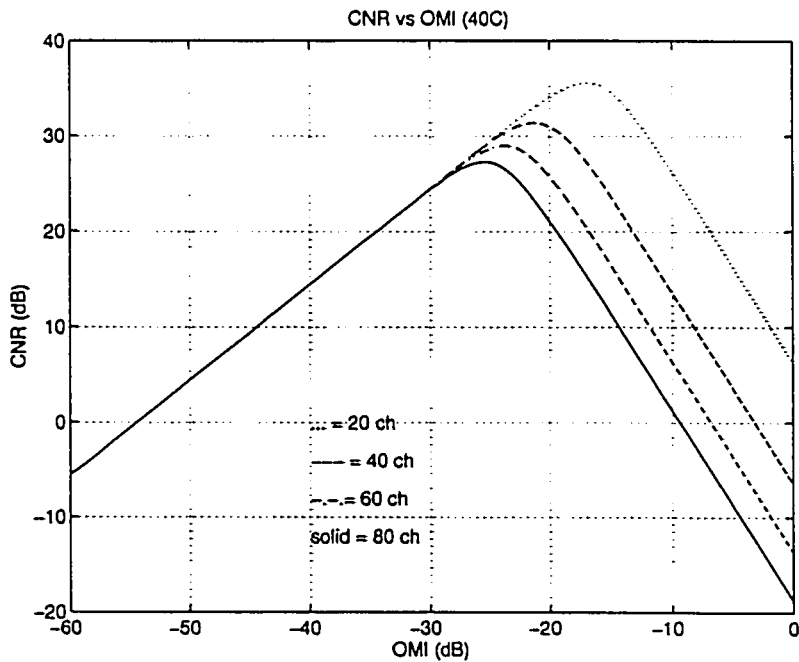


*FIG. 29 CNR of the DM/DD link using OEM at 40 °C*

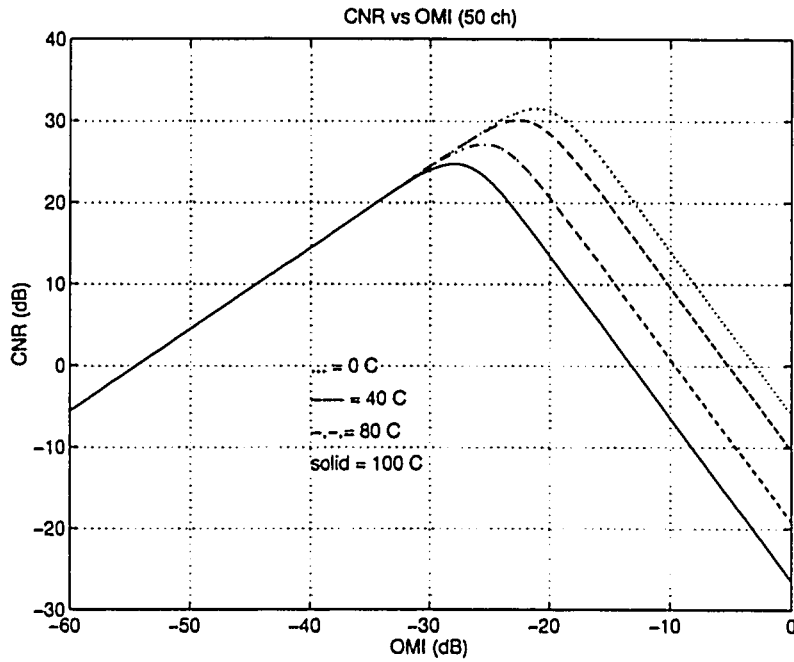


FIG. 30 CNR of the DM/DD link using OEM with temperature as a parameter

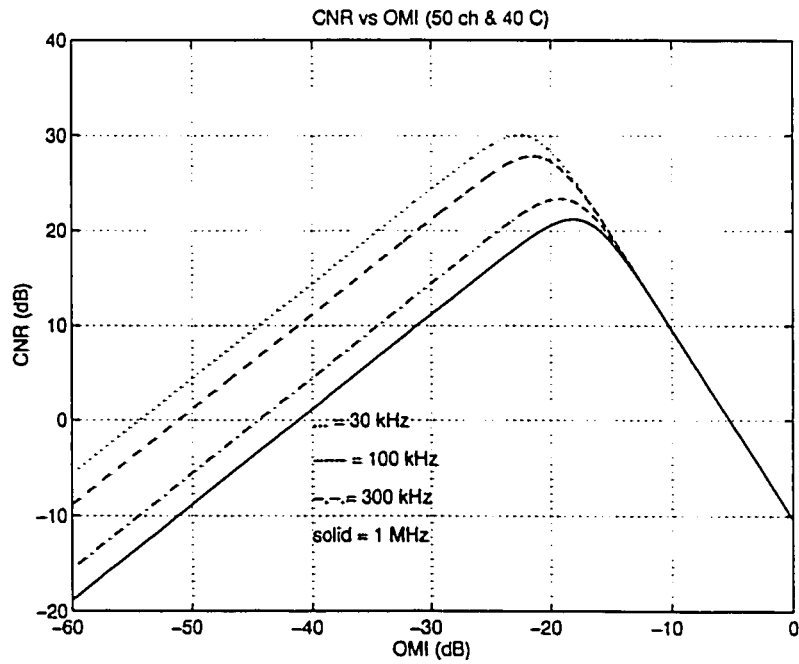


FIG. 31 CNR of the DM/DD link using OEM with channel as a parameter

### 4.3 External modulators loop

In the following analysis, we will consider the loop system with three groups of channels where each group contains three subcarriers shown in FIG. 14. They are classified as group a, b, c and channel 1, 2, 3. A Mach-Zehner interferometer is used as the external optical modulator.

#### 4.3.1 Up-link system

At the output of a Mach-Zehner interferometer, the light intensity can be expressed as [30] :

$$I_o = \frac{I_i}{2} \cdot (1 + \cos \phi) \quad \text{EQ. 31}$$

where  $I_o$  is the output light intensity,  $I_i$  is the input light intensity,  $\phi$  is the input signal to the interferometer;

And  $\phi$  can be expressed as:

$$\phi = \phi_o + \sum_{i=1}^N \frac{\pi V}{V_\pi} \cdot \cos(\omega_i t) \quad \text{EQ. 32}$$

where  $\phi_o$  is the initial phase, N is the number of channels,  $V_\pi$  is the half-wave voltage of the interferometer.

At each EBS, the input light, which already contains the information from the previous RBSs, will be modulated by the radio signals of that station. The output light will contain the information signals, as well as their harmonics and intermodulation products.

At the end of the link, i.e. at the input of the photodetector at the CBS, the optical signal is:

$$I_{out} = I_{phi} \cdot \left( \begin{array}{l} \left\{ 1 - \sin \left[ \frac{\pi V_{a1}}{V_{\pi}} \cdot \cos(\omega_{a1}t) + \frac{\pi V_{a2}}{V_{\pi}} \cdot \cos(\omega_{a2}t) + \frac{\pi V_{a3}}{V_{\pi}} \cdot \cos(\omega_{a3}t) \right] \right\} \cdot \\ \left\{ 1 - \sin \left[ \frac{\pi V_{b1}}{V_{\pi}} \cdot \cos(\omega_{b1}t) + \frac{\pi V_{b2}}{V_{\pi}} \cdot \cos(\omega_{b2}t) + \frac{\pi V_{b3}}{V_{\pi}} \cdot \cos(\omega_{b3}t) \right] \right\} \cdot \\ \left\{ 1 - \sin \left[ \frac{\pi V_{b1}}{V_{\pi}} \cdot \cos(\omega_{b1}t) + \frac{\pi V_{b2}}{V_{\pi}} \cdot \cos(\omega_{b2}t) + \frac{\pi V_{b3}}{V_{\pi}} \cdot \cos(\omega_{b3}t) \right] \right\} \end{array} \right) \quad \text{EQ. 33}$$

where  $I_{phi}$  is the received dc light at the detector and can be expressed as:

$$I_{phi} = \frac{1}{8} I_{dc} \eta L \quad \text{EQ. 34}$$

where  $I_{dc}$  is the dc light output of the laser source at the CBS,  $\eta$  is the responsivity of the photodetector, and  $L$  is the loss of the optical fiber link.

We can expand EQ. 33 in term of Bessel functions using the following identity [31]:

$$\exp(iz \cos \theta) = 1 + 2 \sum_{k=1}^{\infty} i^k J_k(z) \cos(k\theta) \quad \text{EQ. 35}$$

where  $J_k(z)$  is the Bessel function of  $k^{\text{th}}$  order.

After expanding EQ. 33, the optical signal at the fundamental frequency is:

$$I_{sig} = I_{phi} \cdot \frac{J_1(m)}{4} \cdot \cos(\omega t) \quad \text{EQ. 36}$$

where  $m = \frac{\pi \cdot V}{V_{\pi}}$  is the modulation index of the carrier signal.

As explained in section 3, only third order intermodulation products will fall into the information band and distort the data signals. These products contribute to the intermodulation distortion (IMD). There are two types of IMD in this system. One of them results from the channels within one group and it is referred as the intra-group IMD; the other one results from the channels from other groups and is referred as the inter-group IMD. The rms current of the intra-group IMD is:

$$\langle i_{IMD} \rangle_i^2 = \frac{1}{2} \{ 2I_{ph1} [J_1^3(m) + J_1^2(m) \cdot J_3(m) + J_2^2(m) \cdot J_3(m)] \}^2 \quad \text{EQ. 37}$$

and the rms current of the inter-group IMD is:

$$\langle i_{IMD} \rangle_e^2 = \frac{1}{2} \{ 2I_{ph1} [J_1^3(m) + J_1^2(m) \cdot J_3(m)] \}^2 \quad \text{EQ. 38}$$

Now the carrier-to-noise ratio (CNR) can be expressed as:

$$CNR_{up} = \frac{\frac{1}{2} (2I_{ph1} J_1(m))^2}{\left( RIN \cdot I_{ph1}^2 + 2qI_{ph1} + \langle i_{TH}^2 \rangle \right) \cdot BW + \langle i_{IMD} \rangle_i^2 + \langle i_{IMD} \rangle_e^2} \quad \text{EQ. 39}$$

where BW is the bandwidth per carrier, q is the electron charge, RIN is the relative intensity noise for the laser source,  $\langle i_{TH}^2 \rangle$  is the equivalent input noise current density in the receiver.

The CNR of the up-link system is shown in FIG. 32. The parameters used for calculation is listed in TABLE 4.

From EQ. 39, we see that the power of the carrier signal is proportional to  $J_1^2(m)$ , while the power of the third order IMD is proportional to  $J_1^6(m)$ ; therefore, the carrier



to intermodulation ratio is proportional to  $1/J_1^4(m)$ . This expression is similar to the DM/DD link. Therefore, the explanation of the CNR performance in DM/DD link also applies here.

output power of the laser source, $P_o$	0 dBm
photodetector responsivity, $\eta$	0.8 A/W
electron charge, $q$	$1.6 \times 10^{-19}$ C
fiber and coupler loss, $L$	4 dB
$\langle i_{th}^2 \rangle$	$4.0 \times 10^{-22}$ W/Hz
RIN	-150 dB/Hz
half-wave voltage, $V_\pi$	10 V
coupler ratio, $C$	1/3

**TABLE 4. Parameters in calculating CNR of the OEM loop system**

As the number of the RBS increases, the power of the signal will not be degraded except for more coupling loss and fiber loss. However, the CNR will decrease because the power of the third order IMD increases as the number of RBS increases. As a result, the maximum number of RBSs that can be installed is limited.

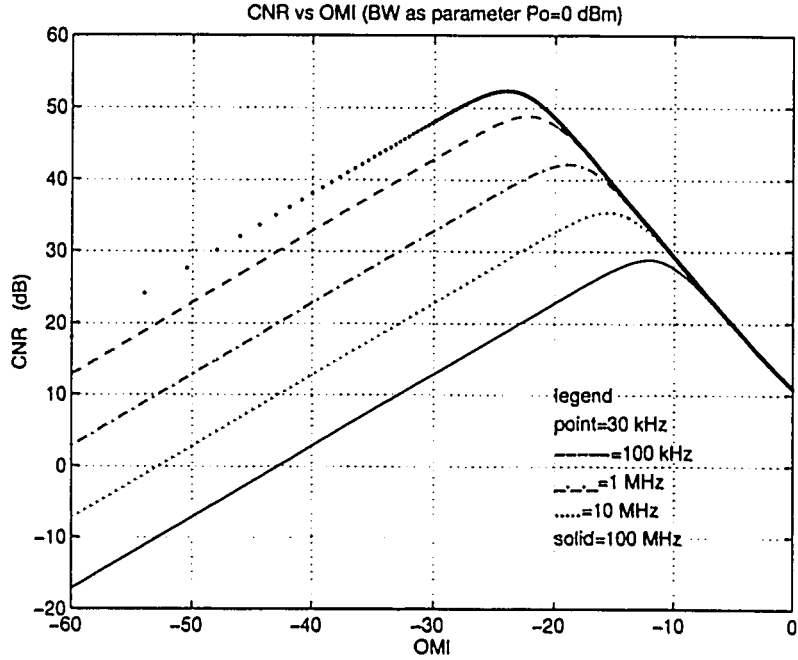


FIG. 32 CNR performance of the up-link system

#### 4.3.2 Down-link system

Unlike the up-link system, all nine carriers will be applied to one EOM at one time in the down-link system. A frequency up-conversion is also performed at the second EOM. With properly graded couplers, each RBS will receive one third of the total light output from the CBS. The detected optical signal at each RBS is:

$$\begin{aligned}
 I_{det} = I_{ph2} \cdot & \left\{ 1 - \sin \left( \frac{\pi \cdot V_{LO}}{V_{\pi}} \cos(\omega_{LO}t) \right) \right\} \\
 & \cdot \left\{ 1 - \sin \left[ \frac{\pi \cdot V_{a1}}{V_{\pi}} \cos(\omega_{a1}t) + \frac{\pi \cdot V_{a2}}{V_{\pi}} \cos(\omega_{a2}t) + \frac{\pi \cdot V_{a3}}{V_{\pi}} \cos(\omega_{a3}t) \right. \right. \\
 & + \frac{\pi \cdot V_{b1}}{V_{\pi}} \cos(\omega_{b1}t) + \frac{\pi \cdot V_{b2}}{V_{\pi}} \cos(\omega_{b2}t) + \frac{\pi \cdot V_{b3}}{V_{\pi}} \cos(\omega_{b3}t) \\
 & \left. \left. + \frac{\pi \cdot V_{c1}}{V_{\pi}} \cos(\omega_{c1}t) + \frac{\pi \cdot V_{c2}}{V_{\pi}} \cos(\omega_{c2}t) + \frac{\pi \cdot V_{c3}}{V_{\pi}} \cos(\omega_{c3}t) \right] \right\}
 \end{aligned} \tag{EQ. 40}$$

where  $V_{LO}$  is the applied voltage of the LO,  $\omega_{LO}$  is the LO frequency, and  $I_{ph2}$  is the received dc photocurrent, and  $I_{ph2}$  can be expressed as:

$$I_{ph2} = \frac{1}{4} I_{dc} \eta LC \quad \text{EQ. 41}$$

where C is the coupling ratio and it is one third in this case.

The signal current at the fundamental frequency in this case will be:

$$I_{sig} = 2 \cdot J_1(m_{LO}) \cdot J_1(m) \cdot I_{ph2} \cdot \cos(\omega t) \quad \text{EQ. 42}$$

where  $m_{LO}$  is the modulation index of the LO and m is the modulation index of the subcarrier. Since all nine carriers are mixed at one EOM, the detailed calculation for expanding EQ. 40 in terms of Bessel functions will be very complicated. However, the power of the IMD resulting from the higher order terms will be very small and can be neglected. Therefore, only third order IMD will be considered here. The rms current of one IMD term is:

$$\langle i_{IMD}^2 \rangle = \frac{1}{2} \left( 2J_1^3(m) J_1(m_{LO}) I_{ph2} \right)^2. \quad \text{EQ. 43}$$

According to R. Gross and R. Olshansky [32], the maximum number of third order products is bounded by  $3N^2/8$ , where N is the number of channels. In this system, there are three channels in each group; therefore, three IMD components will be generated. Similarly, a maximum of three more IMD terms will be generated by the channels from different groups. As a result, the worst case for this system will have six IMD terms. Now the CNR can be expressed as:

$$CNR_{down} = \frac{\frac{1}{2} (2I_{ph2} J_1(m_{LO}) J_1(m))^2}{\left( RIN \cdot I_{ph2}^2 + 2qI_{ph2} + \langle i_{TH}^2 \rangle \right) \cdot BW + 6 \langle i_{IMD}^2 \rangle}. \quad \text{EQ. 44}$$

A similar simulation of CNR performance is carried out for the down-link system and the results is shown in FIG. 33. The parameters used are the same as the up-link system, and the modulation index of the local oscillator signal,  $m_{LO}$ , is set to 1 in FIG. 33. It is also assumed that each RBS will couple an equal amount of power, i.e. for our analysis of a three RBS system, each of the RBSs will couple one third of the total output power from the CBS ( $C=1/3$ ). From FIG. 33, it can be seen that the CNR of the down-link system is lower than the up-link system. It is because the up-converted signal level is lower due to the mixing of the LO signal. From FIG. 34, it can be seen that the maximum CNR achieved will increase as the modulation index of the LO signal increases. When the  $m_{LO}$  is larger, the power of the information signal will be larger. Thus results in a higher CNR.

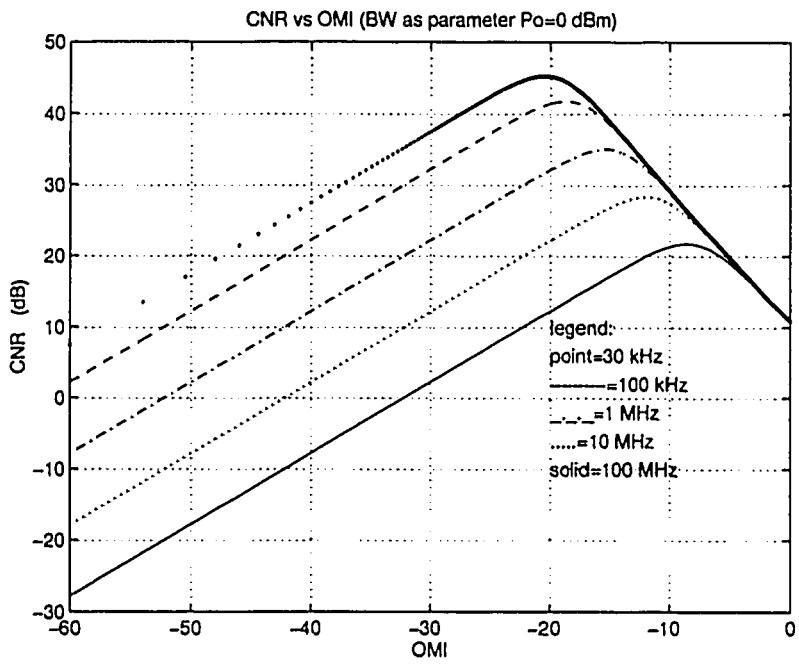


FIG. 33 CNR performance of the down-link system

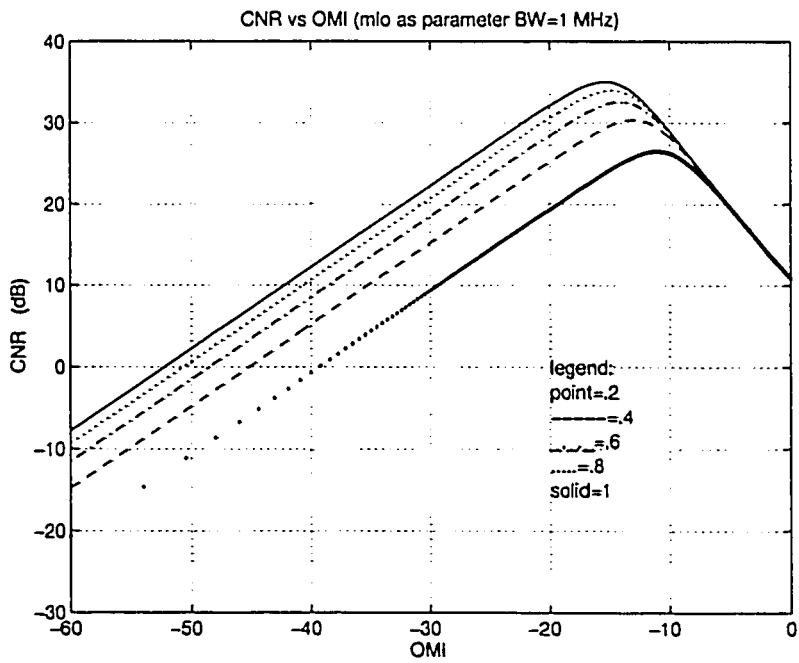


FIG. 34 CNR of the down-link system with  $m_{LO}$  as a parameter

## **5.0 EXPERIMENT RESULTS**

### **5.1 Modulators characteristics**

In this section, the transfer characteristics of the two electro-optic modulators used in the experiment will be examined. The two modulators used are CRC (Communication Research Canada) lightwave testset model PT150 and the 2X2 ETEK Electro-Optic switch.

#### **5.1.1 CRC lightwave testset**

The CRC lightwave testset includes a 1535 nm laser diode and a LiNbO<sub>3</sub> Mach-Zehnder modulator. The laser diode is used to provide an unmodulated continuous source for the Mach-Zehnder modulator. The laser diode is built into the testset and is not available for external adjustment. The operating wavelength of the laser diode is 1535 nm and the threshold current is 13.7 mA. The operating current for this laser diode is set at 53.4 mA which is well beyond the threshold and is in its linear region.

The Mach-Zehnder modulator is made of LiNbO<sub>3</sub>. It is designed to operate at 1550 nm but it works well at 1535 nm too. The transfer characteristic of the modulator is shown in FIG. 35 . From the graph, it can be seen that the half-wave voltage of the modulator is 5.35V. When the modulator is DC biased at around 5 V, a fairly linear transfer characteristic is obtained.

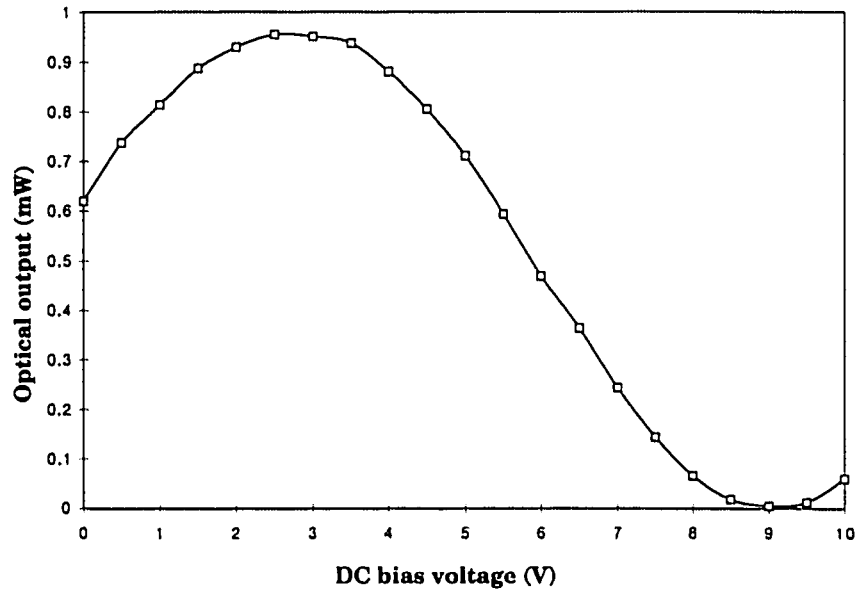


*FIG 35. Transfer characteristic of the CRC testset*

### 5.1.2 ETEK 2X2 electro-optic switch

The other modulator used in the experiment is the ETEK 2X2 electro-optic switch. Its physical structure is a balanced bridge interferometer 2X2 switch shown in FIG. 36 .

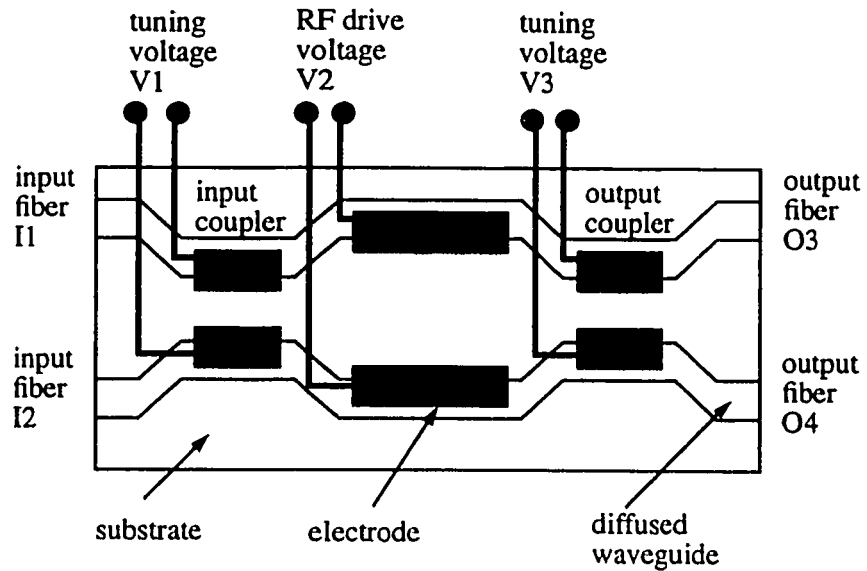


*FIG 36. Physical structure of a balanced bridge interferometer*

The input and output couplers are constructed by placing two waveguides close to each other. A certain amount of optical power can be coupled from one waveguide into another by tuning the voltage settings at the input and the output couplers. When the tuning voltage is applied such that the couplers split the optical power equally, the ETEK 2X2 switch can function similar to a Mach-Zehnder modulator. The specified electrical bandwidth of the switch at the electrical RF input V2 is approximately 7 GHz with a maximum input power rating of 30 dBm. This switch also needs an external DC bias voltage to select the operating point. The transfer characteristic of the switch is shown in FIG. 37 .



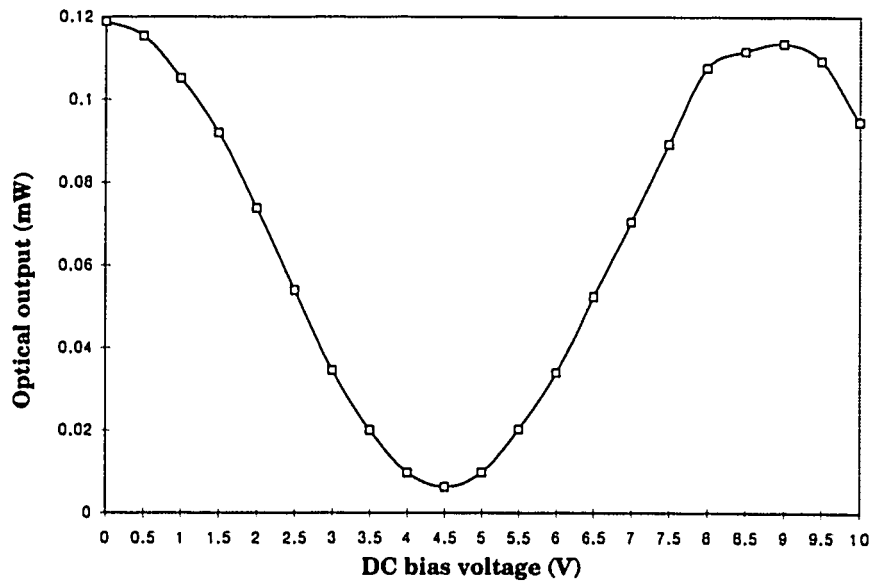


*FIG 37. Transfer characteristic of the ETEK 2X2 electro-optic switch*

From the graph, it can be seen that the half-wave voltage of the switch is about 4.25 V. This switch can be biased at around 2 V or 7 V to obtain a linear operation.

## **5.2 Harmonics generation of the Mach Zehnder modulator**

This test will examine the properties of the harmonic generation of the Mach Zehnder modulator. The experimental setup is shown in FIG. 38 .

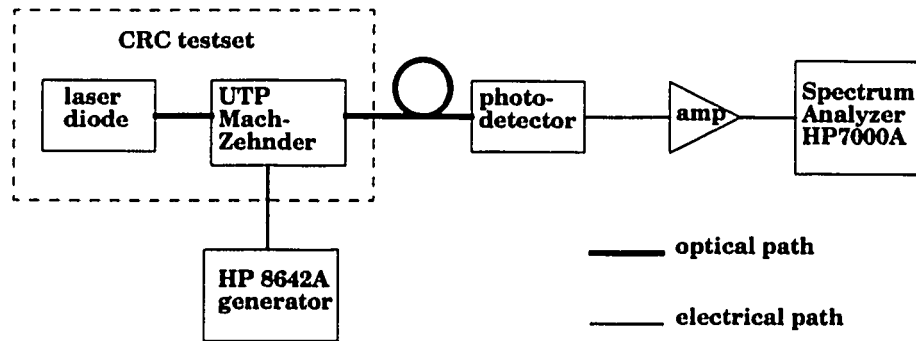
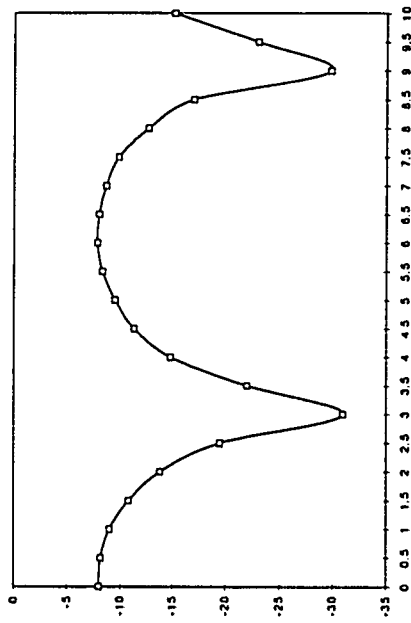
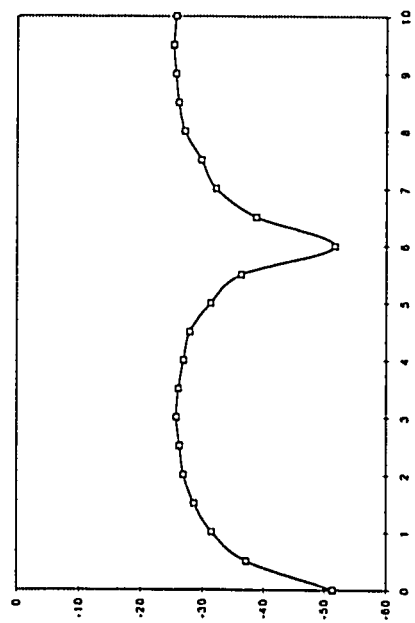


*FIG 38. Experimental setup for harmonic measurement*

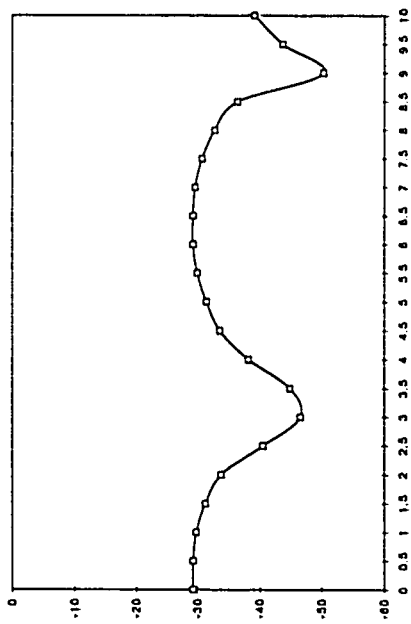
The results of the signal power versus modulator's dc bias voltage are shown in FIG. 39 for the fundamental frequency  $f_1$ , first harmonic  $2f_1$ , second harmonic  $3f_1$  and third harmonic  $4f_1$ . From the graphs, it can be seen that the fundamental signal and the second harmonic vary similarly while the first and third harmonic vary similarly. The fundamental and the second harmonic have maximum power when the modulator is operated at its linear region and have minimum power when the modulator is operated at its most non-linear region (i.e. the maximum and the minimum of the transfer characteristic). The first and the third harmonic, however, have maximum power when the modulator is biased at the most non-linear region and have minimum power when the modulator is biased at the linear region.



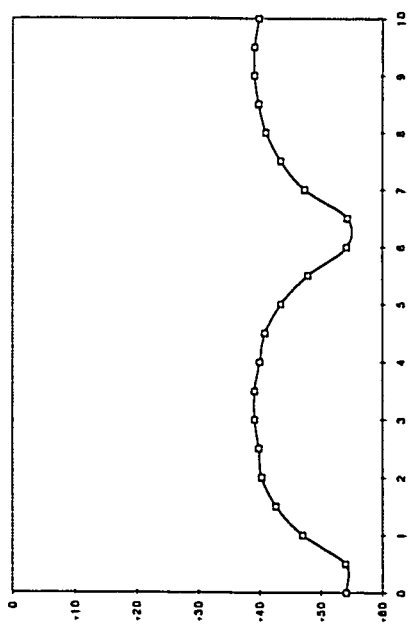
(a)



(b)



(c)



(d)

**FIG 39.** Signal power versus DC bias voltage of the Mach-Zehnder modulator: a) fundamental, b) first harmonic, c) second harmonic, d) third harmonic.

### 5.3 Two cascaded stages test

In this section, the performance of a system consisting two cascaded modulators is examined. This configuration simulates a microwave fiber optic link with two remote antenna sites.

The experimental setup for this test is shown in FIG. 40 .

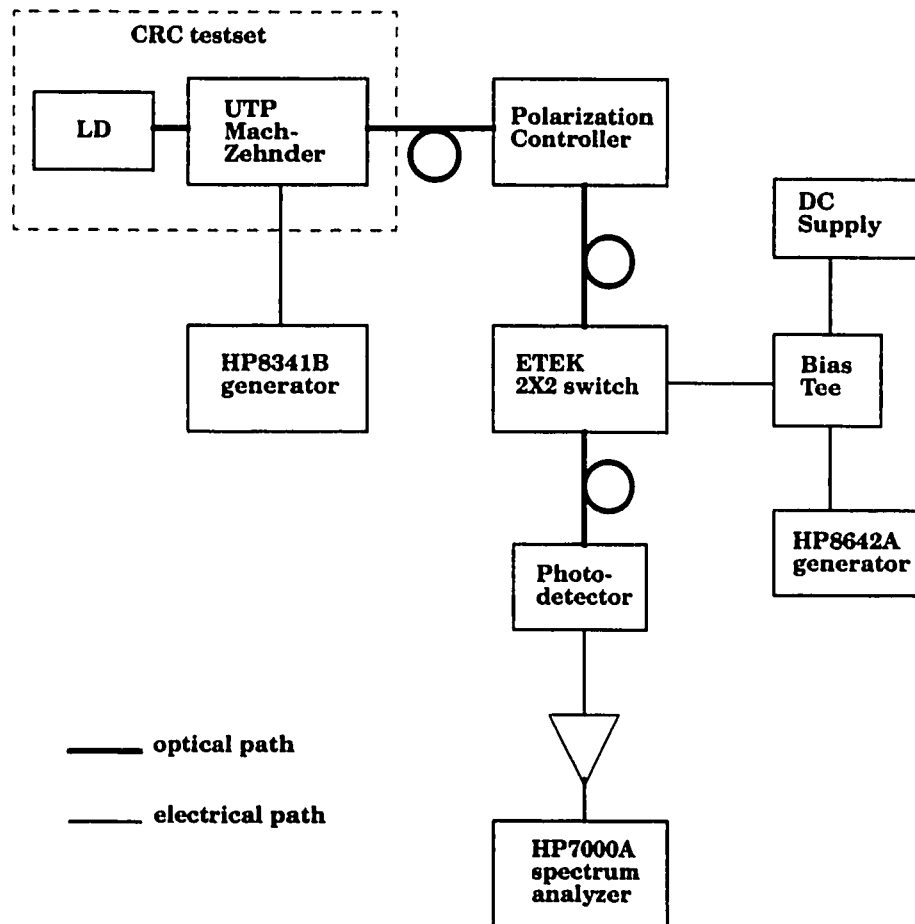


FIG 40. Experimental setup for the two stages test

The laser diode and the first Mach-Zehnder modulator are inside the CRC testset. The forward biasing current for the laser diode is set at 53.4 mA and the optical power at the fiber end is approximately 4.3 mW. An RF signal at 1.2 GHz generated from the HP

8431B generator is coupled into the UTP Mach-Zehnder modulator. Since the CRC testset has a DC biasing circuit built in for the modulator, no DC voltage is allowed at the RF port.

The electro-optic effect in the lithium niobate  $\text{LiNbO}_3$  devices, such as the ETEK 2X2 electro-optic switch, is highly sensitive to the polarization of the input light. The electro-optic effect is approximately three times larger in the TE mode compared to the TM mode. Therefore, in order to maximize the electro-optic effect, the polarization of the input light should be as linear as possible and the axis of the polarization should be oriented so that the TE mode is aligned properly to the applied electric field.

To achieve a linear polarization in the desired direction for the ETEK 2X2 switch, a polarization controller is inserted before it. The controller used for this experiment was a single mode fiber controller constructed at TR Labs according to the direction given in reference [33]. The controller consists of several small loops of fiber and fastened to a rotatable plate. The principle of operation is that the polarization of the light is altered by inducing birefringence in the fiber. Birefringence is accomplished by rotating the plate with loops to place stress on the fiber.

The ETEK switch needs external DC bias; therefore, a bias tee is used to combine the DC voltage and the RF signal generated by the HP8642A before they are applied to the V2 port of the ETEK switch.

At the end, the optical signals are detected by the 143X series photodetector from New Focus where the optical signals are converted to electrical signals. The responsivity of the photodetector module is 6.80 mV/mW. Finally, the electrical signal is amplified and measured by the HP7000A spectrum analyser.

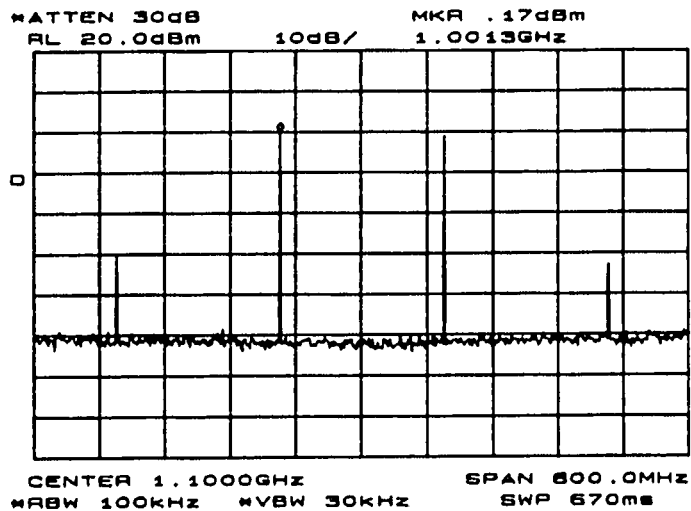
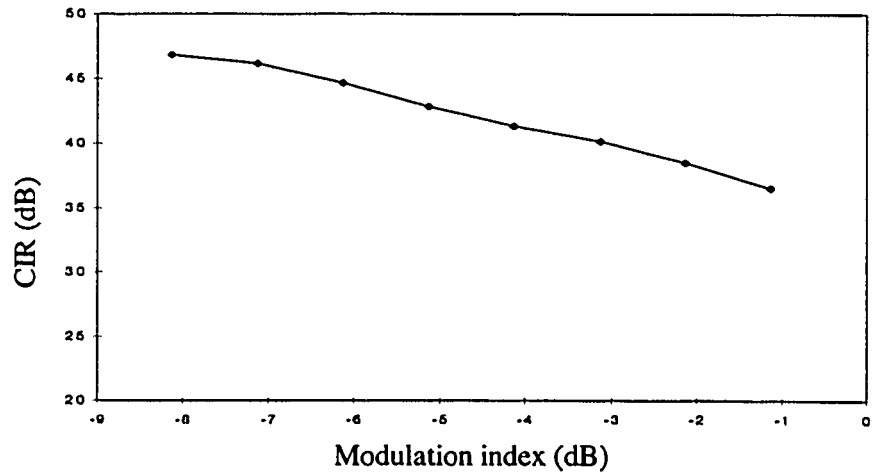


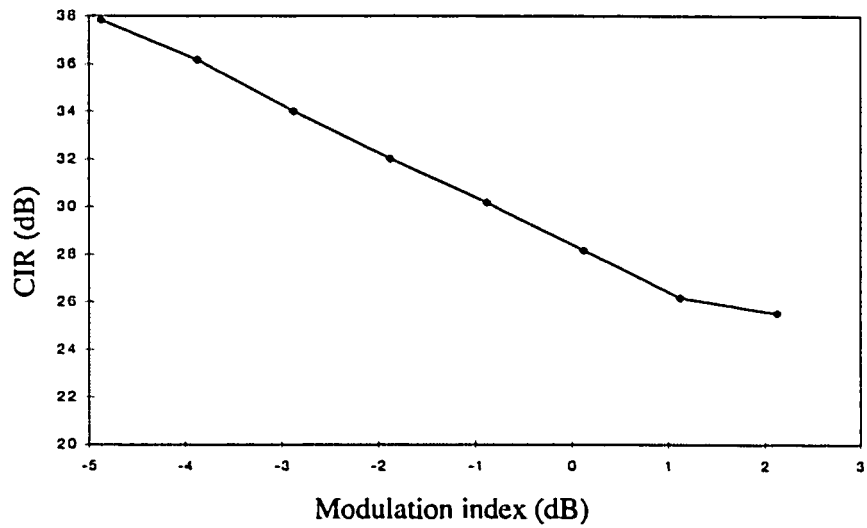
*FIG 41. Frequency spectrum for the two stages test*

The frequency spectrum of the measured signals is shown in FIG. 41 . The spectrum at the detector output consists of two fundamental frequencies at 1.00 GHz (channel 2) and 1.20 GHz (channel 1), the third order intermodulation product at 800 MHz and 1.4 GHz. From FIG. 41 , it can be seen that the carrier-to-noise ratio for the fundamental signal in a 100 kHz noise bandwidth is about 50 dB.

The carrier-to-intermodulation ratio (CIR) is the power ratio between the carrier frequency and the third order intermodulation product as explained in section 4.3 . As shown in FIG. 41 , the CIR is about 30 dB for both channels.



(a)



(b)

*FIG 42. CIR as a function of modulation index (two stages test). (a) channel 1, (b) channel 2*

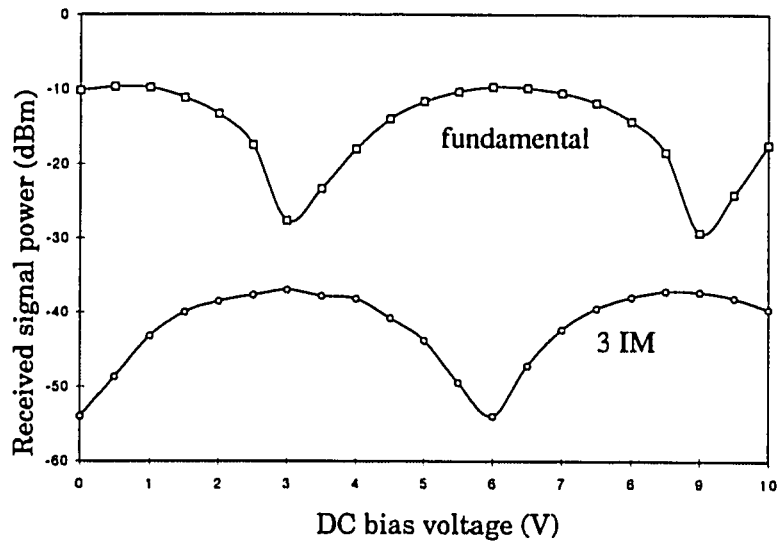
The variation of CIR as a function of modulation index is shown in FIG. 42 . The modulation index is defined as  $\frac{\pi \cdot V}{V_{\pi}}$ , where V is the applied signal voltage and  $V_{\pi}$  is the half-wave voltage of the modulator. The modulation index is the same as that specified in section 4.3 . From section 4.3 , it can be seen that the power of the third order IMD

increases  $J_1^3(m)$  as the power of the carrier frequency. Therefore, the CIR is inversely proportional to  $m^3$  ( $CIR \propto \frac{1}{m^3}$ ). Since the modulation index is less than one, a smaller modulation index will result in a higher CIR. As FIG. 42 shows, the result agrees with the theoretical prediction.

As explained in section 4.3 , the overall carrier-to-noise ratio (CNR) is composed of several components such as RIN noise, shot noise, IMD, etc. Among them, the IMD is the one which dominates at the higher modulation index (<-15dB). The other noises will start to dominate at a lower modulation index. Therefore, there will be a maximum CNR as seen in the simulation results shown in section 4.3.1 . However, due to the limitation of the equipment available, only the results at the higher modulation index can be obtained, and the behaviour of the CNR when dominated by other source of noises cannot be shown.

The Mach-Zehnder modulator is not a linear device, since it has a sinusoidal transfer characteristic and the operating point where the modulator is biased will affect the power of the carrier frequency signals as well as the intermodulation products. Thus it will affect the CIR performance.

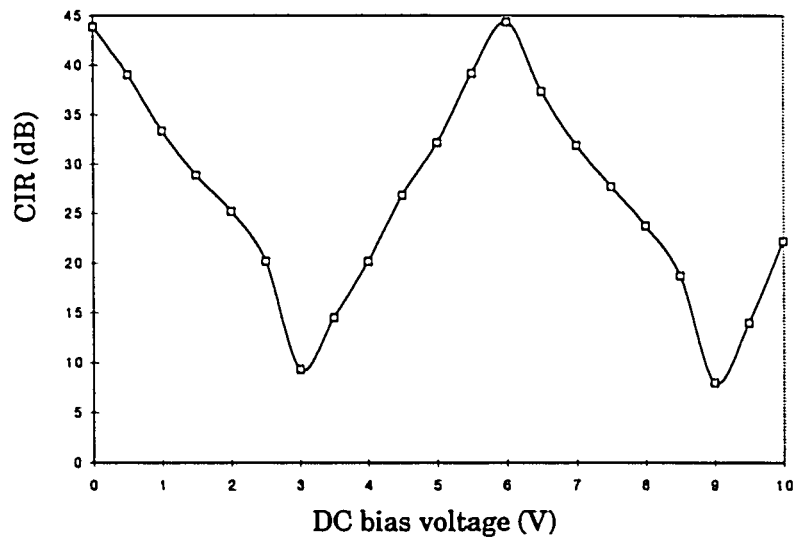




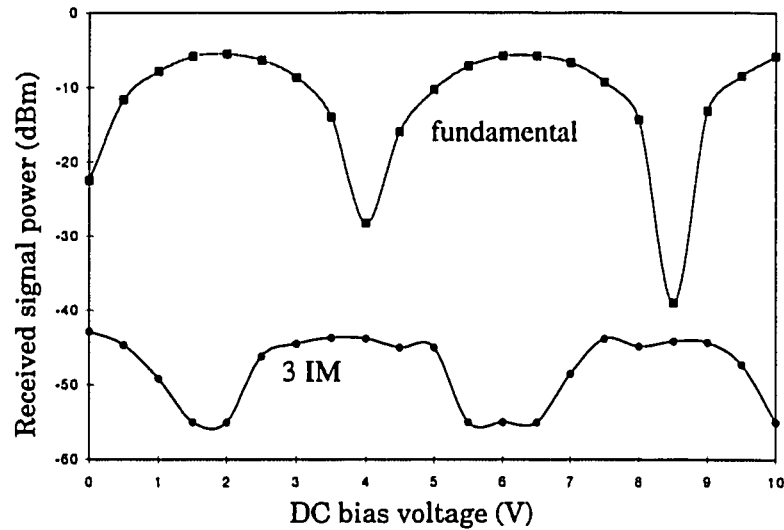
*FIG 43. Power of the channel two signal and the intermodulation product at 1.6 GHz as a function of the DC bias voltage of modulator one.*

FIG. 43 shows the variation of power of the carrier frequency signal at 1.2 GHz (channel two) and the intermodulation product at 1.4 GHz when the DC bias voltage of the modulator one is changing. The 1.2 GHz signal is applied to the first modulator (the CRC testset). The intermodulation products (at 800MHz and 1.4GHz) are the mixing products of the fundamental signal and the first harmonic of the other signal ( $2f_a - f_b$ ). From section 5.1 , it can be seen that the transfer characteristic of the CRC testset reaches its maximum and minimum at 2.5 V and 8.75 V respectively. When the modulator is biased at one of these two voltages, the power of the fundamental frequency (1.2GHz) will be minimum while the power of the first harmonic ( $2f_a = 2.4\text{GHz}$ ) will be maximum. The intermodulation product will also be maximum. On the other hand, when the modulator is biased near 6 V, a fairly linear transfer characteristic is obtained. Thus the power of the fundamental frequency is maximum and the power of the first

harmonic is minimum which results in a minimum power intermodulation product. From FIG. 43 , it can be seen that the power of the carrier frequency reaches minimum at around 3 V and 9 V which are the maximum and the minimum of the transfer characteristic of the modulator. At the same time, the power of the intermodulation product reaches the maximum. As a result, the CIR will be minimum when the modulator is biased at this voltage. When the modulator is biased at around 6 V, the power of the carrier frequency is maximum while the power of the intermodulation product is minimum as shown in FIG. 43 . At this point, the CIR will be maximum. FIG. 44 shows the variation of the CIR for channel two as a function of the dc bias voltage of the first modulator.



*FIG 44. CIR of channel two as a function of DC bias voltage of modulator one.*



*FIG 45. Power of the channel one signal and the intermodulation product at 700 MHz as a function of the DC bias voltage of modulation two.*

The same theory applies to the second modulator (ETEK 2X2 switch). FIG. 45 shows the variation in power of the carrier frequency signal at 1 GHz (channel one) and the intermodulation product at 800 MHz. From FIG. 37, it can be seen that there are two maximum points at 0V and 8.5V and one minimum point at 4V for the transfer characteristic of the ETEK 2X2 switch. Therefore, the channel one fundamental signal will reach a minimum at these three voltages as shown in FIG. 45, and the power of the first harmonic will be maximum. Thus the intermodulation product will reach a maximum at these voltages as seen in FIG. 45. Thus the CIR of channel two is at minimum when the modulator is biased at these voltages. It can also be seen that the channel one fundamental signal will reach a maximum at around 2V and 6.5V which correspond to the linear regions of the transfer characteristic of the ETEK modulator. At these bias voltages, the first harmonic is minimum; therefore, the intermodulation product is at a

minimum and the CIR of channel two is maximized. FIG. 46 shows the CIR of channel one as a function of the dc bias voltage of modulator two.

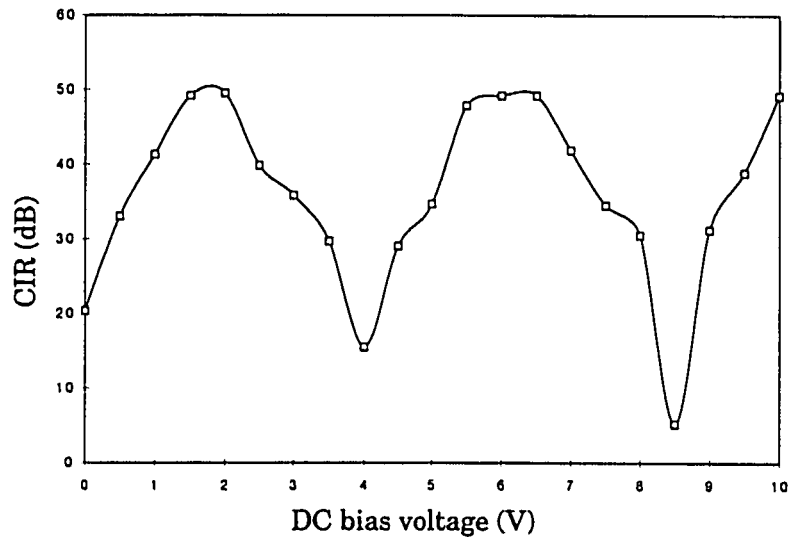


*FIG 46. CIR of channel one as a function of DC bias voltage of modulator two.*

The dynamic range of the fiber optic link is a measure of the variation of signal levels that can be carried by the link. The dynamic range is usually defined as the ratio of the fundamental signal to the third order intermodulation products at a specified input level. Since the power of the intermodulation distortion decreases faster than the power of the fundamental signal, reduction of the input signal power yields a larger value of dynamic range. However, when the input signal power decreases, the signal-to-noise ratio also decreases because the noise floor of the link is constant for a specified noise bandwidth. Thus, there is an input signal level at which the intermodulation distortion level is equal to the noise floor of the link, and at this input level, the dynamic range is maximised. This is referred to as the spurious-free dynamic range (SPDR).

From FIG. 47 , it can be seen that the SPDR for channel 1 is approximately 45 dB and from FIG. 48 , the SPDR for channel 2 is approximately 40 dB.

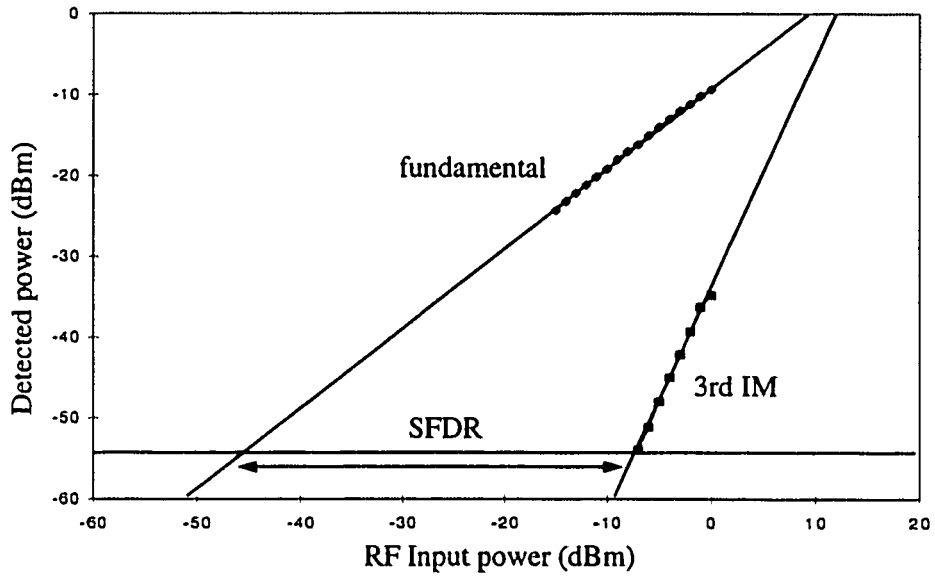


FIG 47. SPDR for channel one

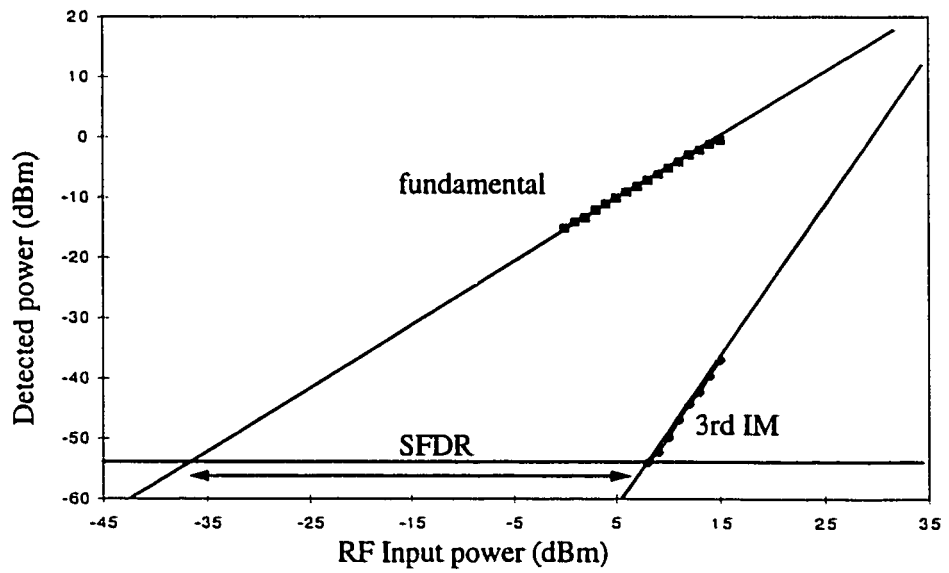
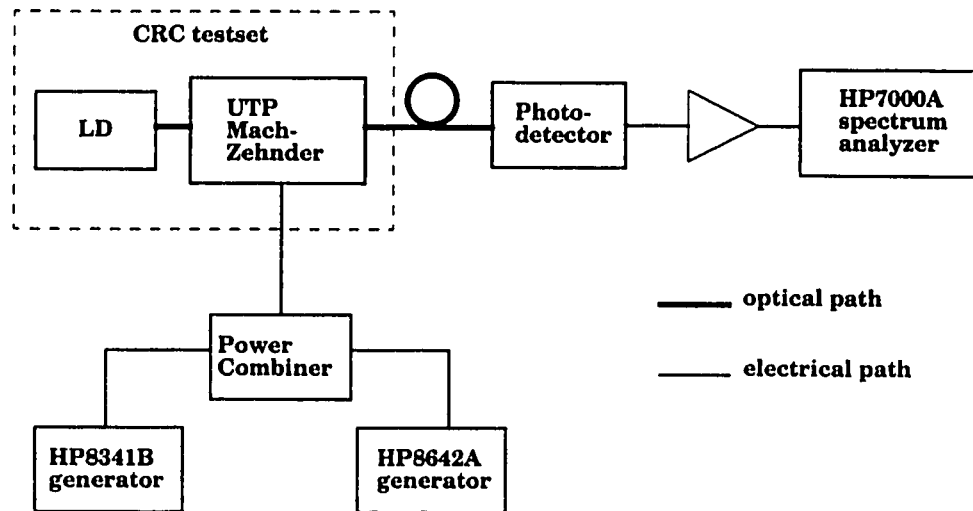


FIG 48. SPDR for channel two

## 5.4 Single stage test

This test will examine the performance of a single modulator system with two carrier frequencies and this emulates a single antenna site with two user channels. The experimental setup is shown in FIG. 49 .



*FIG 49. Experimental setup for single stage test*

The power combiner is used to add two single frequency signals generated by HP8431B and HP8642A signal generators, and the combined signal is connected to the RF input port of the CRC testset. The output light from the Mach-Zehnder modulator will be intensity modulated by the combined RF signal. At the end, the optical signals will be detected by the New Focus 141x photodetector. Finally, the signals are examined using the HP7000A spectrum analyser.

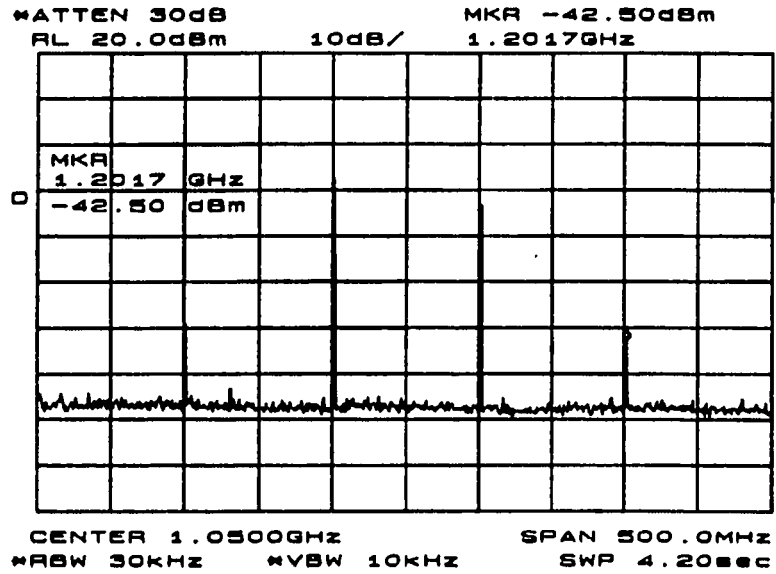


FIG 50. Frequency spectrum of the single stage test

FIG. 50 shows the frequency spectrum of the detected signal. This spectrum is very similar to spectrum of the detected signal of the two-stage test. There are two fundamental carrier frequencies at 1 GHz and 1.1 GHz and the intermodulation products at 900 MHz and 1.2 GHz. The signal to noise ratio for the fundamental carrier frequency in a 30 kHz noise bandwidth is about 50 dB. The noise floor for the system is about -58dBm.

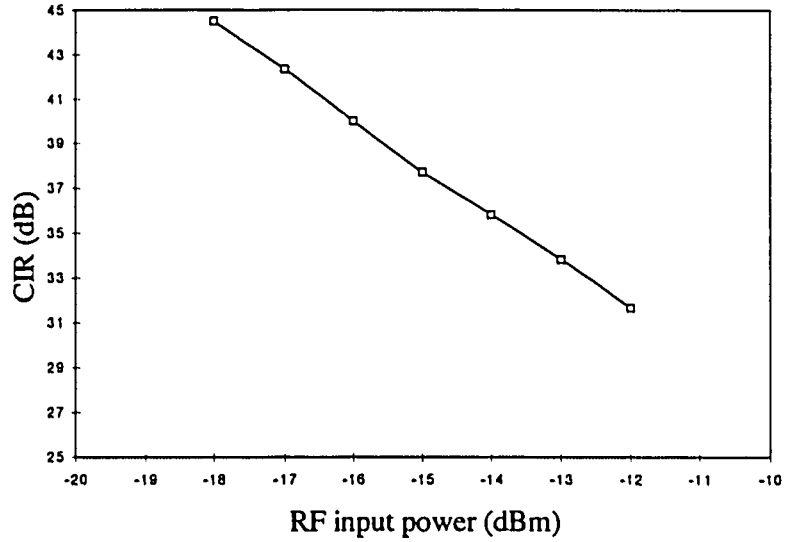


FIG 51. CIR of channel one versus RF input power (single stage test)

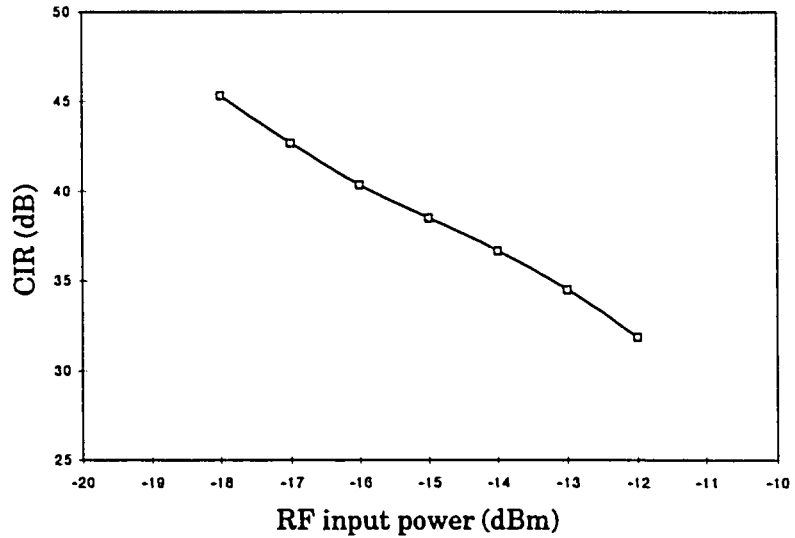


FIG 52. CIR of channel two versus RF input power (single stage test)

The variation of CIR as a function of RF input power for channel one and two are shown in FIG. 51 and FIG. 52 respectively. The CIR increases as the RF input power decreases. The RF input power is linearly proportional to the modulation index.



Therefore, the CIR increases when the modulation index decreases. Once again, the results in the graphs agree with the theory stated in section 4.3 .

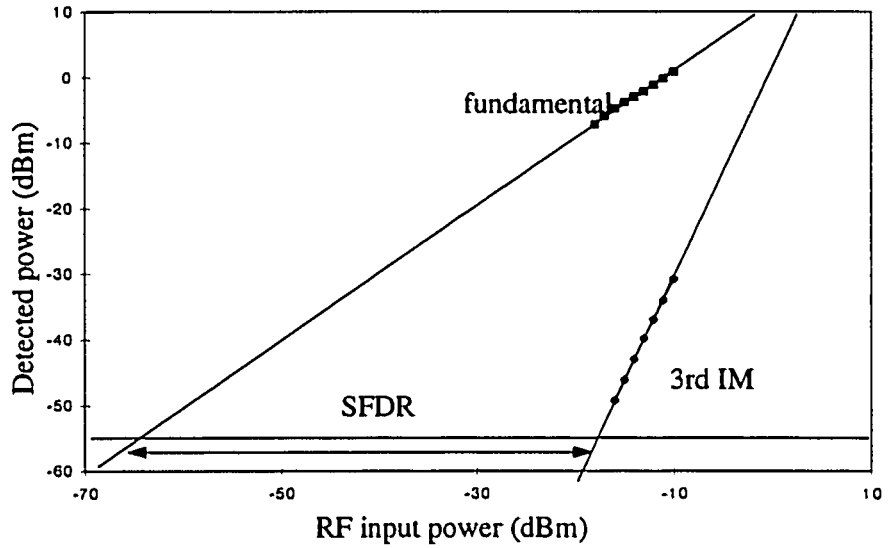


FIG 53. SPDR of channel one. (single stage test)

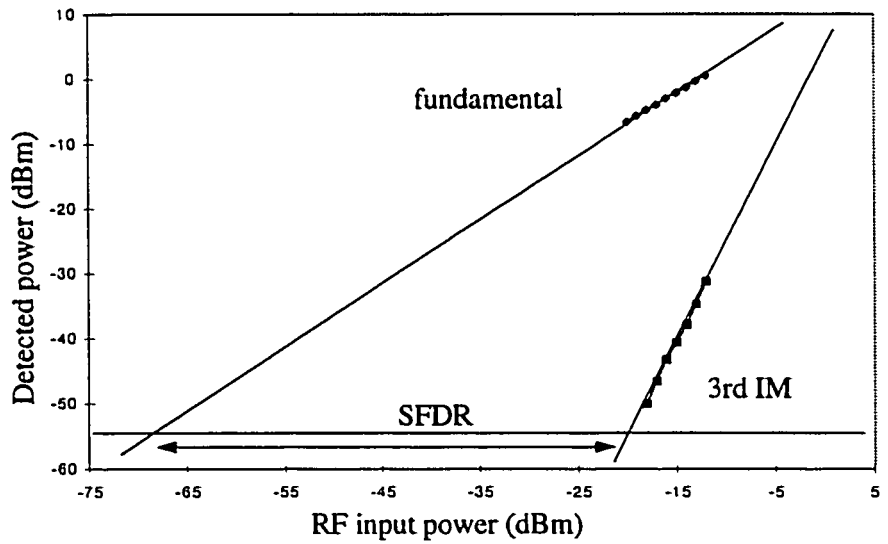
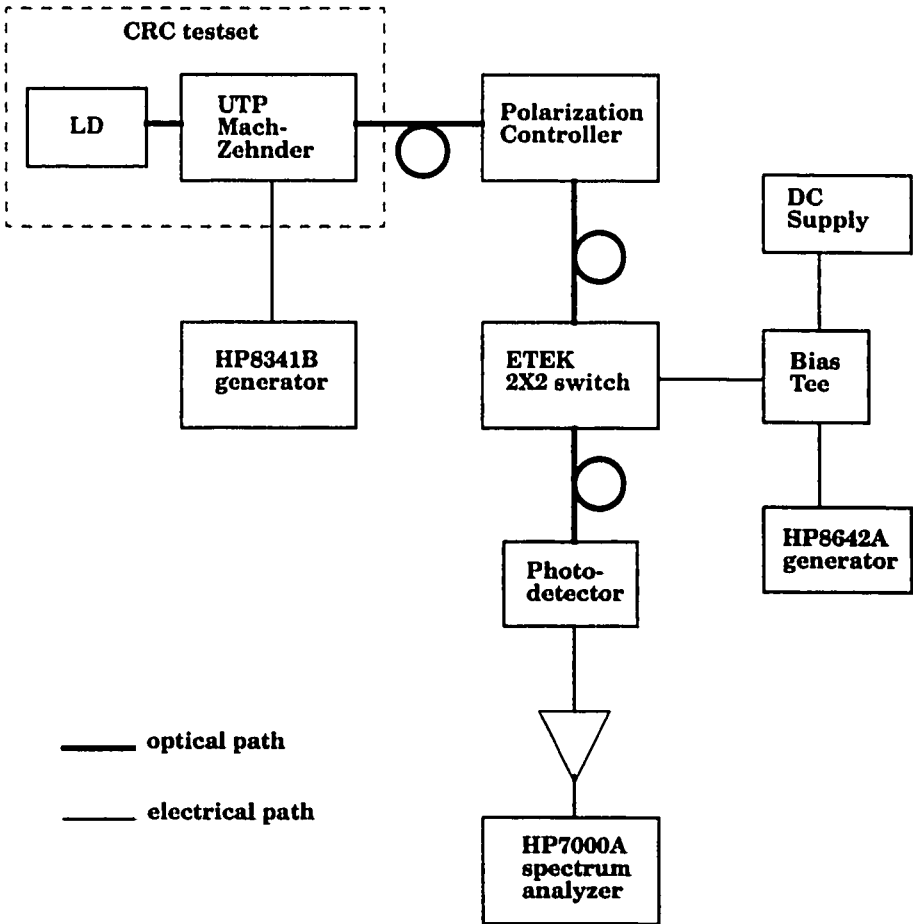


FIG 54. SPDR of channel two. (single stage test)

The dynamic ranges for channel one and channel two are shown in FIG. 53 and FIG. 54 respectively. The SFDR for channel one is approximately 48 dB and the SFDR for channel two is approximately 47 dB. Since this is a single stage test, both channels experience the same distortion and noise. Therefore, the SFDR for either channels is approximately the same.

### 5.5 Mixing properties

This test will examine the mixing properties of a system consisting of two modulators. A Mach-Zehnder modulator can be used as a mixer to perform frequency up-conversion and down-conversion. The experimental setup is shown in FIG. 55 .



*FIG 55. Experimental setup for frequency conversion measurement*

The setup is exactly the same as the two-stage test. This time, a 1GHz signal and a 1.3GHz signal are applied to the first and the second modulator respectively. However, instead of examining the fundamental signals, the powers of the frequency up-converted signal and frequency down-converted signal are examined. FIG. 56 shows the spectrum of the detected signal from 100MHz to 3GHz. The spectrum consists of many signals: the frequency down-converted signal at 300MHz, the frequency up-converted signal at 2.3GHz, the intermodulation products at 700MHz and 1.6GHz, the channel one signal at 1GHz and its first harmonic at 2GHz, the channel two signal at 1.3GHz and its first harmonic at 2.6GHz.

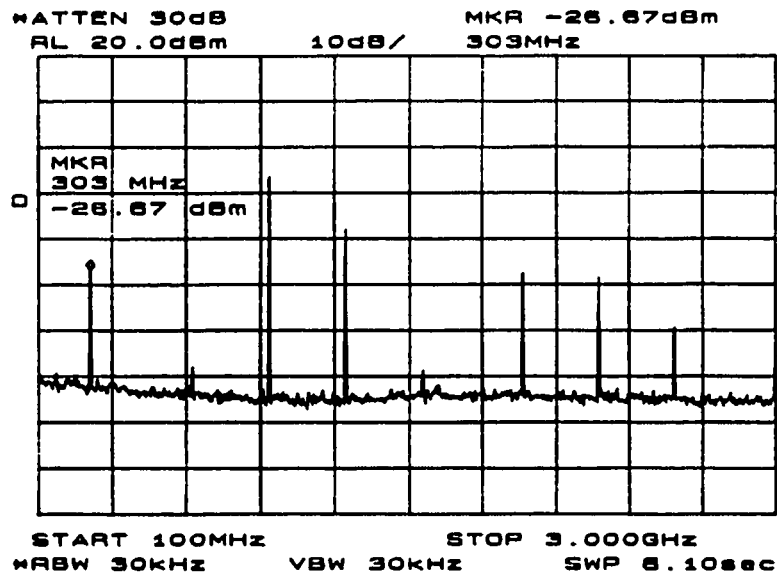


*FIG 56. Frequency spectrum of the frequency conversion test.*

The power of the frequency down-converted signal and the power of the frequency up-converted signal versus the DC bias of the modulator are shown in FIG. 57 and

FIG. 58 respectively. The down-converted signal at 300 MHz and the up-converted signal at 1.6GHz are the mixing products of the two fundamental signals. The fundamental signals have the strongest power level at around 6V where the modulator is operated at its linear region. Thus the up and down-converted signals will be strongest at this bias voltage. From FIG. 57 , it can be seen that a maximum occurs at around 6V.

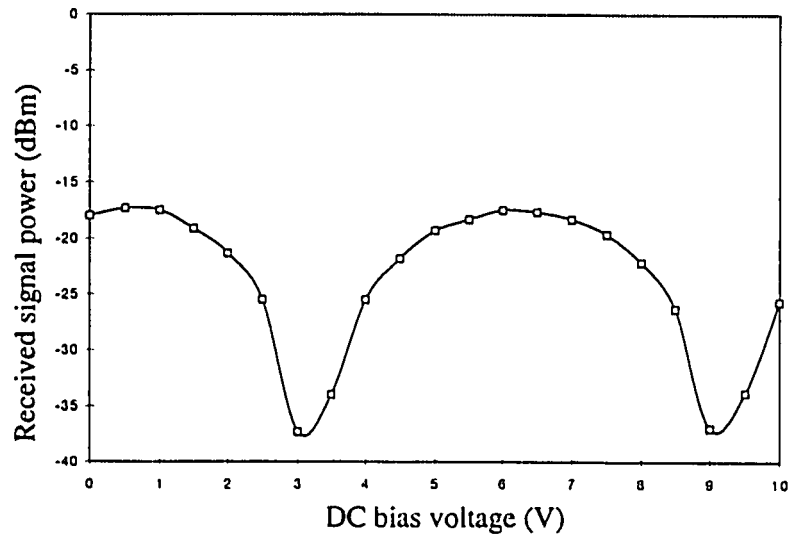


*FIG 57. Power of frequency down-converted signal as a function of DC bias voltage of the modulator. (RF input 0 dBm and 15 dBm)*

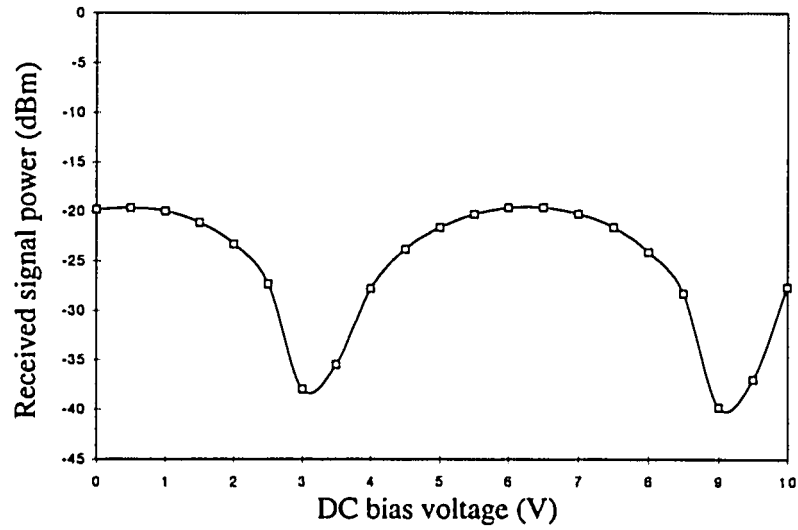


*FIG 58. Power of frequency up-converted signal as a function of DC bias voltage of the modulator. (RF input 0 dBm and 15 dBm)*

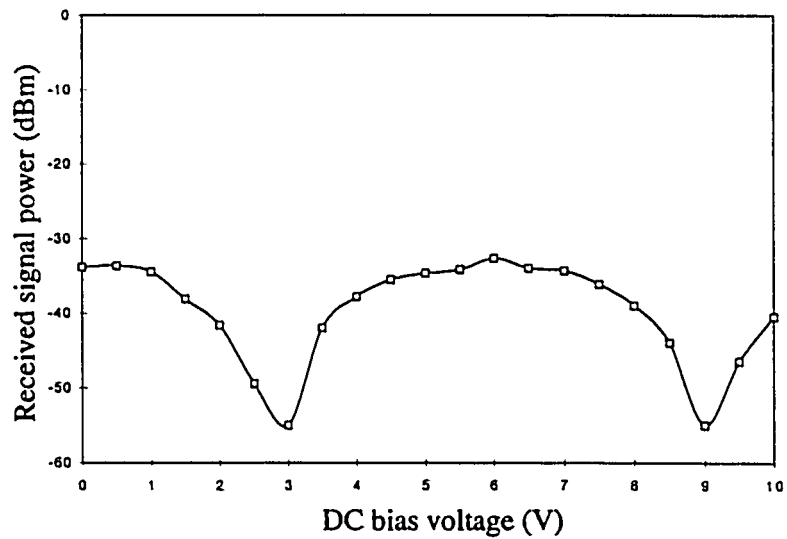


*FIG 59. Power of frequency down-converted signal as a function of DC bias voltage of the modulator. (RF input -15 dBm and 10 dBm)*

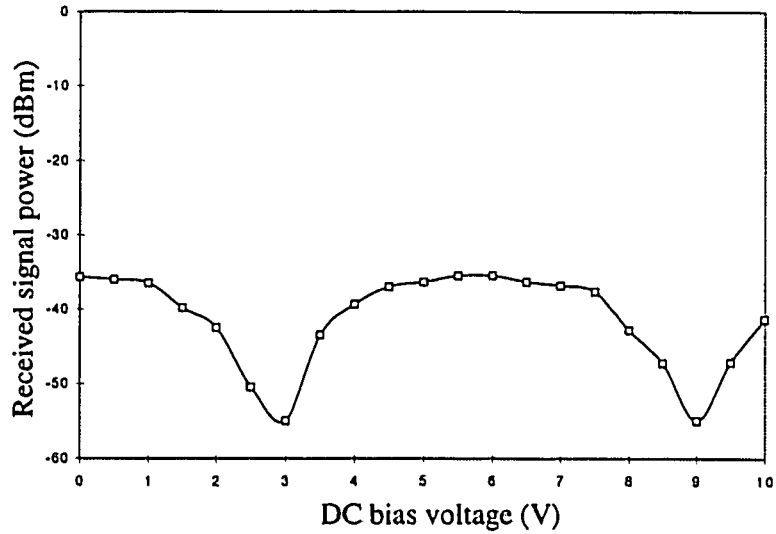


*FIG 60. Power of frequency up-converted signal as a function of DC bias voltage of the modulator. (RF input -15 dBm and 10 dBm)*

FIG. 59 and FIG. 60 show the power of the up- and down-converted signals versus the DC bias of the modulator with lower RF input power. From the graphs, it can be seen that the signal powers are lower. However the variation of the signal powers are similar to those with higher RF input power.

## 5.6 Summary

The transfer characteristics of the two modulators have been investigated. The half-wave voltages ( $V_{\pi}$ ) are 5.35 V and 4.25 V for the CRC testset and the ETEK 2X2 electro-optic switch respectively. The fundamental and the even order harmonics signals are strong when the Mach Zehnder modulator is biased at the linear region and the odd harmonics are strong when the modulator is biased at the non-linear regions such as maximum and minimum peaks of the transfer characteristic. In the two-stage experiment, it is seen that the CIR is higher when the modulation index is lower. The

dynamic ranges for channel one and channel two are 48 dB and 40 dB respectively. It is also seen that the maximum CIR is obtained when the modulator is biased at the linear region. This is because the fundamental signal will be at maximum while the third order intermodulation product is at minimum when the modulator is biased at the linear region. In the single stage test, it is also seen that the CIR is higher when the modulation index is lower. The dynamic ranges for both channels are about 47 dB. In the mixing properties test, it is seen that the modulators need to be biased at the linear region to obtain a maximum frequency up- and down-converted signal.

## 6.0 ECONOMIC ANALYSIS ON THE PROPOSED LINKS

One of the main considerations for choosing which system to deploy is the cost. In this chapter, a more detailed examination from the economic point of view is discussed.

### 6.1 Physical layout

A system consisting 19 cells is used to illustrate the difference of the total fiber length in the cascaded modulators loop system and the direct link system.

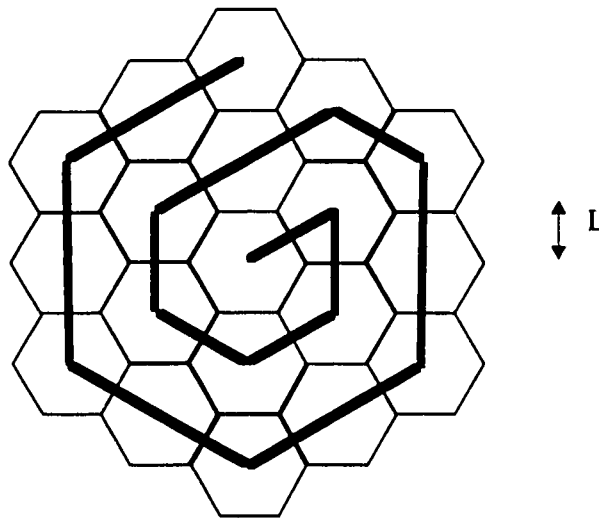


*FIG 61. Physical layout of the cascaded modulators loop system.*



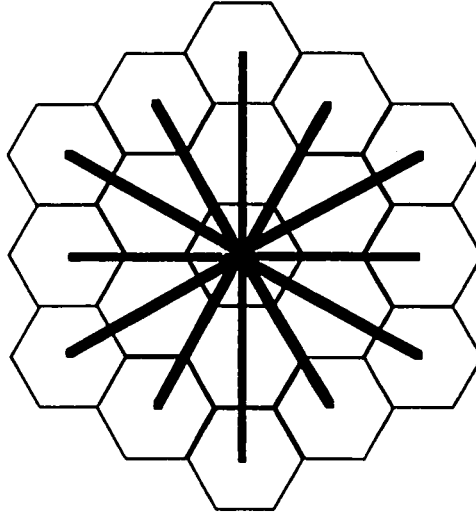


*FIG 62. Physical layout of the direct link system.*

FIG. 61 shows the physical layout of the fiber cables in the cascaded modulator loop system and FIG. 62 shows the physical layout of the fiber cables in the direct link system.

In the calculation of the total length of the fiber cables, it is assumed that the antenna is located at the center of each site. All the cells except the first and the last one are simple remote antenna sites containing no expensive control circuitries. It is also assumed that the perpendicular distance from the edge of the cell to the center of the cell is  $L$ . From FIG. 61, it can be seen that the total length of the fiber cables needed in the cascaded modulator loop system is:

$$18 \times 2 \times L = 36L.$$

If the last cell is connected to the first cell to centralize all the control equipment in one cell site, an additional fiber cable of  $3.464L$  is required and the total length of the fiber cable will be  $39.464L$ .

For the direct link system, the total length of the fiber cables required will be:

$$6 \times 4L + 6 \times 2L + 6 \times 3.464L = 56.7846L.$$

It can be seen that the direct link system requires almost 40% more fiber cables than the cascaded modulator loop system. It is not only that the cost of the required fiber cables increases but the cost for the installation of the fiber cables also increases. In a compact city, especially in the city center area, the installation cost for fiber cable will be very high. The cascaded modulator loop will be more attractive than the direct link system. If the cost for installation of the fiber cables per unit length is the same for both system, the setup cost for the direct link system will be 40% more expensive.

## **6.2 Number of components**

Another factor which affects the cost of the system is the number of components to be installed. It will require more money to install more components at the initial setup (both cost and installation) and also to maintain the system afterward.

For the cascaded modulator loop system, the components required to realize the system described in the previous section are:

1 laser, 19 optical couplers, 20 external optical modulators, 20 photodetectors, 4 optical amplifiers (assuming one optical amplifier is required for every 5 cascaded stages), 1 multiplexer and encoder, 1 demultiplexer and decoder.

The total number of components required for the cascaded modulator loop system is therefore 66.

The number of antennas and electrical amplifiers is the same for the two systems. Therefore, they are not included in the cost comparison.

For the direct link system using MSM photodiodes, the components required are:

38 laser diodes, 19 optical couplers, 38 photodiodes, 19 local oscillators, 19 electrical mixers, 38 band pass filters and 19 MSM photodiodes.

The total number of the components required for the direct link system is 152.

It can be seen that the direct link system requires 130% more components than the cascaded modulator loop system. Although the costs of the systems cannot be directly compared as the components are different, the direct link system will still be more expensive than the cascaded modulator loop system. For a system with large number of cell sites, the cascaded modulator loop system is more attractive than the direct link system.

## **7.0 CONCLUSION**

Future microcellular communication systems and personal communication systems require a large number of cells to cover the service area. It will be very expensive for each cell to have all the control and logic equipment installed. The cost for the system would be greatly reduced if all these equipment can be centralized in one location and that leads to the idea of antenna remoting. A transmission medium with low cost and noise is needed to carry the information between the central base station and the remote antenna sites and microwave fiber optic links seem to be a good solution.

### **7.1 Thesis review**

This thesis discusses and compares different types of microwave optic links that can be used for future microcellular systems. In chapter 1, an introduction to the development and concept of the cellular communication is given.

In chapter 2, we have presented many types of microwave fiber optic links that can be used for the microcellular systems, including direct modulation/ direct detection (DD/DM) fiber optic link, DD/DM fiber optic links with frequency conversion at the receiver site, externally modulated/ direct detection fiber optic link, fiber optic mixing links. Two systems of analysis are also proposed: a DD/DM system using an optoelectronic mixer (OEM) and a cascaded modulator loop system.

In chapter 3, the theories of different optical components are discussed. We model the transfer characteristics of the laser diode with a new approach. Instead of modelling the whole transfer characteristic curve, we use a curve fitting method to model the stimulated emission part of the transfer characteristic. This method will give a more accurate result since we don't have to model the abrupt transition of the curve when the laser diode switches to stimulated emission from spontaneous emission. We also find that

the third order coefficients increase as the operating temperature increases. This will increase the noise power due to IMD and thus degrade the system CNR. The principle of operation for the external modulator and photodetectors is included and a noise analysis is also presented.

In chapter 4, an investigation on the CNR performance of DM/DD link (link #1) and the DM/DD link using MSM photodiodes for frequency up-conversion (link#2) is carried out. For the system operated at 40 C, the peak CNRs are 65 dB and 36 dB for link#1 and link#2, respectively. The degradation of CNR in link#2 is due to the conversion loss and the insertion loss of the MSM photodiode. We also find that the peak CNR will improve with fewer channels in the system, lower operating temperature, and smaller channel bandwidth. The CNR will also improve with a higher output from the laser diode.

Then, a fiber optic microcellular system using cascaded external optical modulators is studied. Again, the performance of the system is measured as CNR. For the system with 1 MHz bandwidth, a 42dB CNR is achieved in the up-link system while a 35 dB CNR is achieved in the down-link system. The additional 7 dB loss is due to one additional insertion loss of the EOM and coupling loss. The intermodulation distortion will increase with the number of RBSs as well as the number of channels, which eventually limits the size of the system. With this configuration, an inexpensive and compact radio base station can be used. Compared to the star configuration, the number of the fiber optic cables installed is reduced and the cost of the system is reduced.

In chapter 5, the experimental results are presented. We have investigated the transfer characteristics of the two modulators used in the experiment. The properties of harmonic generation of the Mach-Zehnder modulator is included. We have also investi-

gated the carrier-to-intermodulation ratio (CIR) performance and the dynamic range of a system with two cascaded modulators and a single stage system. The dynamic ranges for the two-stage system are 45dB and 40 dB for channel one and channel 2, and for a single stage system, the dynamic range is 48 dB for both channels.

In chapter 6, an economic discussion of the two proposed systems is presented. The economic evaluation is based on the total physical length of fiber cables required and the total number of components installed for both systems in a same size serving area. In both cases, the cascaded modulator loop system has a lower cost.

## **7.2 Future works**

Much future research can be done on personal communication technology. Digital analysis can be performed. Other multiple access schemes such as code division multiple access (CDMA), time division multiple access (TDMA) can also be considered. As the technology of monolithic microwave integrated circuit (MMIC) advances, work on larger scale integration to include all the major components at a receiver site onto one chip should be carried out.

Microcellular communication systems and personal communication systems are increasing in popularity in modern society. Microwave fiber optic links play an important role in making possible a low cost and reliable system. As the technology advances, we should see that microwave fiber optic links will continue to be important.

## 8.0 REFERENCES

- [1] L.J. Greenstein et al., "Microcells in Personal Communications Systems", IEEE Communications Magazine, pp. 76-88, December 1992.
- [2] T.S. Chiu and M.J. Gans, "Fiber Optic Microcellular Radio", Proc. 41<sup>st</sup> IEEE Vehicular Technology Conf., pp. 921-924, June 1991.
- [3] H. Ogawa, D. Polifko and S. Banba, "Millimeter-Wave Fiber Optics Systems for Personal Radio Communication", IEEE Transactions on Microwave Theory and Techniques, vol. 40, no. 12, pp. 2285-2293, December 1992.
- [4] R. Simons, Optical Control of Microwave Devices, pp. 122, Artech House, 1990.
- [5] J.J. Pan, "Laser Mixer for Microwave Fiber Optics", Proc. SPIE, vol. 1217 Signal Processing for Phased-Array Antennas II, pp.46-58, 1990.
- [6] H. Ogawa and Y. Kamiya, "Fiber Optic Microwave Transmission Using Harmonic Laser Mixing, Optoelectronic Mixing, and Optically Pumped Mixing", IEEE Transaction on Microwave Theory and Techniques, vol. 39, no. 12, December 1991.
- [7] H. Ogawa, "Microwave and Millimeter-Wave Fiber Optic Technologies for Sub-carrier Transmission Systems", IEICE Trans. Communications, vol. E76-B, no. 9, September 1993.
- [8] R.S. Tucker and I.P. Kaminow, "High Frequency Characteristics of Directly Modulated InGaAs Ridge Waveguides and Buried Heterostructure Lasers", Journal of Lightwave Technology, vol. 2, pp. 385-393, 1984.
- [9] K. Noguchi, H. Miyazawa and O. Mitomi, "75 GHz Broadband Ti:LiNbO<sub>3</sub> Optical Modulator with Ridge Structure", Electronics letters, vol. 30, no. 12, 1994.

- [10] S. Malone et al., "MMIC Compatible Lightwave and Microwave MIXing Techniques", IEEE Microwave Theory Tech.-S Int. Microwave Symp., pp. 757-760, 1992.
- [11] E. Suematsu and N. Imai, "Signal to NOise Performance of a Fiber Optic Sub-carrier Link Using an HBT Optoelectronic Upconverter", IEEE Microwave Theory Tech.-S Int. Microwave Symp., pp. 1501-1504, 1994.
- [12] Q.Z. Liu and R.I. MacDonald, "Controlled Nonlinearity Monolithic Integrated Optoelectronic Mixing Receiver", IEEE Photonic Technology Letters, vol. 5, no. 12, pp. 1403-1406, 1993.
- [13] Q.Z. Liu and R.I. MacDonald, "A Simple and Cost-effective Fiber Optic Microwave Link with Monolithic Integrated Optoelectronic Mixing Receiver", Proc. of 6th Int. Conf. on Wireless Communications, pp. 250-256, 1994.
- [14] R. Simons, Optical Control of Microwave Devices, pp. 142, Artech House, 1990.
- [15] G.B. Lochart, "A Spectral Theory for Hybrid Modulation", IEEE Transactions on Communications, vol. COM-21, n.7, pp. 790-800, July 1973.
- [16] R. Simons, Optical Control of Microwave Devices, pp. 143.
- [17] H.W. Yen and M.K. Barnoski, "Optical Injection Locking and Switching of Transistor Oscillators", Applied Physics Letters, vol. 32, no. 3, pp.182-184, February 1978.
- [18] H.W. Yen, "Optical Injection Locking of Silicon IMPATT Oscillators", Applied Physics Letters, vol. 36, no. 8, pp. 680-683, April 1980.



- [19] P.R. Herczfeld et al., "Indirect Subharmonic Optical Injection Locking of a Millimeter-Wave IMPATT Oscillator", *IEEE Transactions on Microwave Theory Tech.*, vol. MTT-34, no. 12, pp. 1371-1375, December 1986.
- [20] K. Petermann, "Theoretical Analysis of Spectral Modulation Behaviour of Semi-Conductor Injection Lasers", *Opt. Quantum Electron.*, no. 10, pp. 133-142, 1978.
- [21] C. Lin, *Optoelectronic Technology and Lightwave Communication System*, pp. 301, Van Nostrand reinhold, 1989.
- [22] G.H.B. Thompson, "Temperature Dependence of Threshold Current in GaInAsP DH Lasers at 1.3 and 1.5  $\mu\text{m}$  wavelength", *IEE Proc.*, vol. 128, pt. I, no. 2, pp. 37-43, April 1981,
- [23] D.M. Byrne and B.A. Keating, "A Laser Diode Model Based on Temperature Dependent Rate Equations", *IEEE Photonic Technology Letters*, vol. 1, no. 11, 1989.
- [24] R.I. MacDonald and B.E. Swekla, "Frequency Domain Optical Reflectometer Using a GaAs Optoelectronic Mixer", *Appl. Opt.*, vol. 29, no. 31, pp. 4578-4582, 1990.
- [25] Q.Z. Liu and R.I. MacDonald, "Sensitivity Analysis of Integrated InGaAs MSM-PD's and HEMT Optoelectronic Receiver Array", *IEEE Trans. on Electronic Devices*, vol. 42, no. 7, pp. 1221-1226, 1995.
- [26] R.P. Kodaypak, "An Optoelectronic Mixer for Fiber-Radio Microcell Systems", M.Sc. Thesis, 1996.

- [27] J.Lipson et al., "High-Fidelity Lightwave Transmission of Multiple AM-VSB NTSC Signals", *IEEE Trans. Microwave Theory Tech.*, vol. 38, no.5, pp. 483-492, 1990.
- [28] H. Harada et al., "Performance Analysis of Fiber Optic Millimeter-Wave Band Radio Subscriber Loop", *IEICE Trans. Communications*, E76-B, no.9, 1993.
- [29] R.J. Wescott, "Investigation of Multiple F.M./F.D.M. Carriers through a Satellite T.W.T Operating near to Saturate", *Proc. IEE*, vol. 114, no. 6, pp. 726-740, June 1967.
- [30] B.E.A. Saleh and M.C. Teich, Fundamentals of Photonics, pp. 703, John Wiley & Sons, Inc, 1991.
- [31] G. Ryzhik, Table of Integrals, Series, and Products, pp. 973, 1965.
- [32] R. Gross and R. Olshansky, "Multichannel Coherent FSK Experiments Using Subcarrier Multiplexing Techniques", *Journal of Lightwave Technology*, vol. 8, no. 3, 1990.
- [33] B.G. Koehler and J.E. Bowers, "In-Line Single-Mode Fiber Polarization Controller at 1.55, 1.30 and 0.63  $\mu\text{m}$ ", *Applied Optics*, vol. 24, no. 3, pp. 349-353, February 1985.

## 9.0 APPENDIX

### Appendix A: Derivation for the transfer characteristics of laser diodes

We start from EQ. 3 and EQ. 4. When the laser diode is at steady state, the rate equations become:

$$0 = -\frac{g_o(N_o - N_t)S_o}{1 + \epsilon S_o} + \frac{I_o}{qV} - \frac{N_o}{\tau_n}$$

$$0 = \left( -\frac{g_o S_o}{1 + \epsilon S_o} - \frac{1}{\tau_n} \right) N_o + \frac{I_o}{qV} + \frac{g_o S_o N_t}{1 + \epsilon S_o} \quad \text{EQ. 45}$$

and Eqn 4 becomes:

$$0 = \frac{\Gamma g_o(N_o - N_t)S_o}{1 + \epsilon S_o} - \frac{S_o}{\tau_p} + \frac{\beta \Gamma N_o}{\tau_n}$$

$$0 = \left( \frac{\Gamma g_o S_o}{1 + \epsilon S_o} + \frac{\beta \Gamma}{\tau_n} \right) N_o - \frac{S_o}{\tau_p} - \frac{\Gamma g_o S_o N_t}{1 + \epsilon S_o}$$

$$N_o = \frac{\frac{S_o}{\tau_p} + \frac{\Gamma g_o S_o N_t}{1 + \epsilon S_o}}{\frac{\Gamma g_o S_o}{1 + \epsilon S_o} + \frac{\beta \Gamma}{\tau_n}} \quad \text{EQ. 46}$$

Sub EQ. 46 into EQ. 45,

$$\left( \frac{S_o}{\tau_p} + \frac{\Gamma g_o S_o N_t}{1 + \epsilon S_o} \right) \left( \frac{g_o S_o}{1 + \epsilon S_o} + \frac{1}{\tau_n} \right) = \left( \frac{\Gamma g_o S_o}{1 + \epsilon S_o} + \frac{\beta \Gamma}{\tau_n} \right) \left( \frac{I_o}{qV} + \frac{g_o S_o N_t}{1 + \epsilon S_o} \right)$$

Expand and rearrange, we get:

$$S_o^2 \left( \frac{g_o}{\tau_p} + \frac{\epsilon}{\tau_n \tau_p} \right) + S_o \left( \frac{\Gamma g_o N_t}{\tau_n} + \frac{1}{\tau_n \tau_p} - \frac{\Gamma g_o I_o}{qV} - \frac{\beta \Gamma I_o \epsilon}{qV \tau_n} - \frac{\beta \Gamma g_o N_t}{\tau_n} \right) - \frac{\beta \Gamma I_o}{qV \tau_n} = 0 \quad \text{EQ. 47}$$

## Appendix B: Derivation for the output light versus input current curve

We start with EQ. 21. Combining EQ. 22 and EQ. 21, we get:

$$P = P_o \left( 1 + \frac{c_1}{P_o} i + \frac{c_2}{P_o} i^2 + \frac{c_3}{P_o} i^3 + \dots \right) \quad \text{EQ. 48}$$

and

$$i = \sum_{n=1}^N I_n \cos(\omega_n t).$$

Let  $m_i = \frac{I_i}{P_o}$ , and sub into EQ. 48, we get:

$$P = P_o \left( 1 + c_1 \sum_{n=1}^N m_n \cos(\omega_n t) + \frac{c_2}{P_o} i^2 + \frac{c_3}{P_o} i^3 + \dots \right)$$

Let  $I = \sum_{n=1}^N m_n \cos(\omega_n t)$ , and we will get

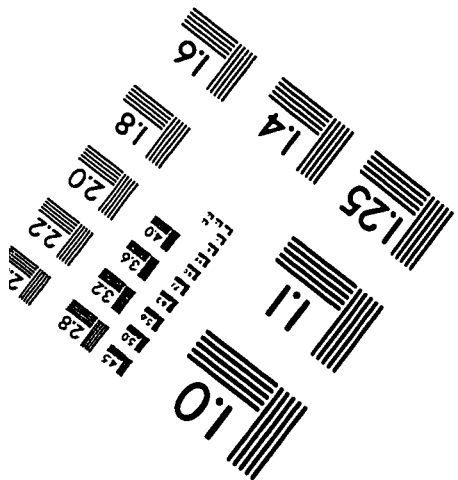
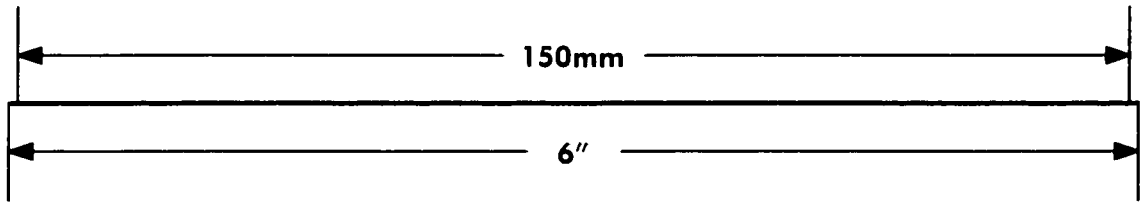
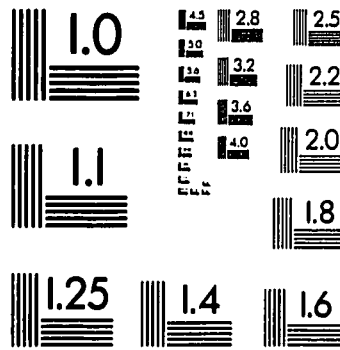
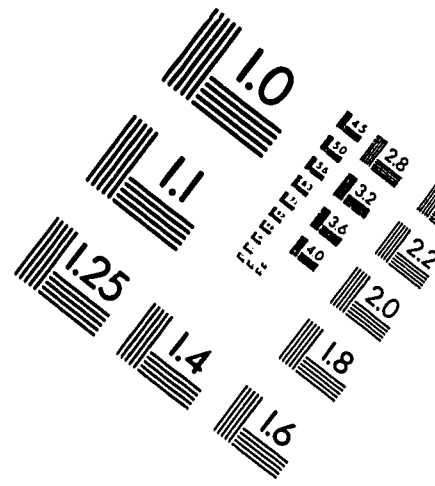
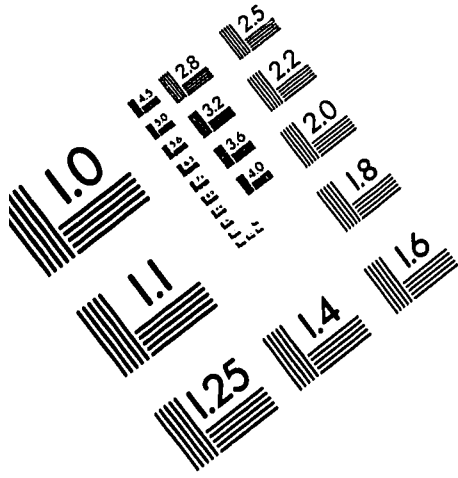
$$\begin{aligned} \frac{c_2}{P_o} i^2 &= \frac{c_2}{P_o} \left( \sum_{n=1}^N I_n \cos(\omega_n t) \right)^2 \\ &= \frac{c_2}{P_o} P_o^2 \left( \frac{1}{P_o} \sum_{n=1}^N I_n \cos(\omega_n t) \right)^2 \\ &= c_2 P_o I^2 = a_2 I^2 \end{aligned}$$

And

$$\frac{c_3}{P_o} i^3 = \frac{c_3}{P_o} \left( \sum_{n=1}^N I_n \cos(\omega_n t) \right)^3$$

$$\begin{aligned} &= \frac{c_3}{P_o} P_o^3 \left( \frac{1}{P_o} \sum_{n=1}^N I_n \cos(\omega_n t) \right)^3 \\ &= c_3 P_o I^3 = a_3 I^3 \end{aligned}$$

# IMAGE EVALUATION TEST TARGET (QA-3)



**APPLIED IMAGE, Inc**  
1653 East Main Street  
Rochester, NY 14609 USA  
Phone: 716/482-0300  
Fax: 716/288-5989

© 1993, Applied Image, Inc., All Rights Reserved

